Label-free detection and profiling of individual solution-phase molecules

2

35

36

3 4 **Authors** Lisa-Maria Needham^{1,2,†}, Carlos Saavedra¹, Julia K. Rasch¹, Daniel Sole-Barber¹, Beau S. 5 Schweitzer¹, Alex J. Fairhall¹, Cecilia H. Vollbrecht^{1††}, Sushu Wan¹, Yulia Podorova¹, Anders 6 J. Bergsten¹, Brandon Mehlenbacher¹, Zhao Zhang³, Lukas Tenbrake⁴, Jovanna Saimi¹, Lucy 7 C. Kneely¹, Jackson S. Kirkwood¹, Hannes Pfeifer⁴, Edwin R. Chapman³, Randall H. 8 Goldsmith1* 9 10 *Corresponding author. Email: rhg@chem.wisc.edu 11 12 **Affiliations** ¹ Department of Chemistry, University of Wisconsin-Madison, WI, USA 13 14 ² Yusuf Hamied Department of Chemistry, University of Cambridge, Cambridge, UK 15 ³ Howard Hughes Medical Institute and the Department of Neuroscience, University of 16 Wisconsin-Madison, WI, USA 17 ⁴ Institut für Angewandte Physik, Universität Bonn, Wegelerstr. 8, 53115 Bonn, Germany 18 †Present Address: School of Biological Sciences, Anatomy Building, Cambridge, UK 19 †† Present Address: Department of Chemistry and Biochemistry, Kalamazoo College, 20 Kalamazoo, MI, USA 21 22 23 The vast majority of chemistry and biology occurs in solution, where conformational 24 dynamics and complexation underly behavior and function. Single-molecule 25 techniques¹ are uniquely suited to resolving molecular diversity, and new label-free 26 approaches are reshaping the power of single-molecule measurements. A label-free 27 single-molecule method ^{2–16} capable of revealing details of molecular conformation in solution^{17,18} would allow a new microscopic perspective of unprecedented detail. 28 29 Here, we use the enhanced light-molecule interactions in high-finesse fiber-based 30 Fabry – Pérot microcavities 19-21 to detect individual biomolecules as small as 1.2 kDa, 31 a ten-amino acid peptide, with signal-to-noise ratios >100, even as the molecules are 32 unlabeled and freely diffusing in solution. Our method delivers 2D intensity and 33 temporal profiles, enabling the distinction of sub-populations in mixed samples. 34 Strikingly, we observe a linear relationship between passage time and molecular

radius, unlocking the potential to gather crucial information about diffusion and

solution-phase conformation. Furthermore, mixtures of biomolecule isomers of the

same molecular weight and composition but different conformation can also be resolved. Detection is based on the creation of a novel molecular velocity filter window and a dynamic thermal priming mechanism that leverage the interplay between optical and thermal dynamics ^{22,23} and Pound – Drever – Hall cavity locking to reveal molecular motion even while suppressing environmental noise ²⁴. New *in vitro* ways of revealing molecular conformation, diversity, and dynamics can find broad potential for applications in life and chemical sciences.

Introduction

Tools to measure properties of individual molecules ¹, including in heterogeneous solutions, have become cornerstones of modern molecular and biomolecular research. Nearly all single-molecule approaches use extrinsic labels, and while these labels provide important contrast and specificity ²⁵, label-free approaches that avoid arduous dye labeling procedures which may perturb the native functionality of biomolecules ^{26–28} are an increasingly desirable alternative. Most single-molecule approaches, including all current label-free methods, also rely on interaction with surfaces. While the presence of a surface may be benign for many applications (such as molecular detection and mass determination), for others, the measurement may bias detection towards sub-populations in mixed samples, disrupt native molecular interactions, and alter dynamics and conformation relative to the solution-phase properties ^{18,29,30} (Supplementary Information). Here, we report a label-free single-molecule technique that enables detection of small solution-phase biomolecules (down to 1.2 kDa) with unprecedented signal-to-noise ratio (SNR) and allows for resolution of their diffusion behavior.

Many label-free single-molecule experiments emphasize molecular detection, whereby the presence of a single copy of a specific molecule is perceived, typically via a surface-bound, selective, tight binder like an antibody. Other approaches emphasize molecular property assaying and extract information about the molecule, such as location, mass, or spectroscopic profile. Property assays are typically incapable of unambiguously identifying the molecule but can be applied generally, whereas molecular detectors can provide selective identification, but only for a small subset of chosen molecules.

The gamut of label-free single-molecule technologies has grown substantially, particularly across two modalities: interference-based and optical microcavity-enhanced techniques. Interferometric measurements, which generally rely on interference between elastically scattered light and a local oscillator, can operate as molecular detectors ^{2,3} or property assays capable of quantitatively determining position ^{4–6} and mass ⁷ of single

molecules. Dielectric optical microcavities provide enhanced light-matter interactions due to high quality factor (Q) and low mode volume (V) 8,9,31. Microcavities have most commonly been applied as molecular detectors, where plasmonic enhancement 10-12, optomechanical coupling ¹³, or a combination of frequency locking and computational noise suppression ¹⁴ have enabled single-molecule detection via the reactive sensing mechanism ³² where the molecule introduces a shift in the resonance frequency. Selectivity is provided by a surfacesupported binder molecule, though the microcavity is sensitive to the presence of molecules even without this step. Microcavities can also be used as single-particle property assays providing details on size and shape ^{33,34} or spectral information on electronic ³⁵, plasmonic ³⁶, or vibrational properties ³⁷, and dynamics ³⁸. However, these approaches require target molecules to be confined or surface-immobilized to allow signal integration and background subtraction, be bound by a surface-supported selective binder, or require interaction with a surface to couple to evanescent modes 18,29. Open-access Fabry – Pérot microcavities can mitigate these concerns by operating in solution ¹⁹ but have not reached the single-molecule label-free regime. Advances include successful single-nanoparticle optical trapping in planoconcave cavities ³⁹ and, the recent demonstration of high-finesse fiber-based Fabry – Pérot microcavities (FFPCs) ²⁰ as highly effective sensors for detecting individual diffusing solution-phase silica nanoparticles ²¹. By monitoring frequency shift, formation of higherorder spatial modes, and changes in transmission intensity, the nanoparticle position was tracked and diffusion information was calculated ²¹. Here, we take advantage of the openaccess geometry of FFPCs to achieve sensing of single, freely diffusing small biomolecules. Our platform utilizes passive mechanical stabilization of FFPCs ⁴⁰, a new dynamic thermal priming mechanism, and active resonance frequency-stabilization as a novel form of molecular velocity filtering, to achieve detection of a 10 amino-acid, 1.2 kDa solution-phase single-protein with SNR of up to 123. This observation is achieved in the absence of external surface-based signal multipliers like plasmonic enhancement and is the highest SNR reported for label-free single-molecule sensing by a substantial margin. Most importantly, the method operates without interaction with surfaces, allowing label-free interrogation of solution-phase molecules and evaluation of molecular diffusion profiles, a carrier of key information on conformation and binding 41.

Results

74

75

76 77

78

79

80

81

82

83 84

85

86

87 88

89

90 91

92

93

94

95

96

97

98

99

100

101

102

103

104105

106

107

108109

110

The FFPC was assembled from two single-mode optical fibers with concave laser-ablated end facets (Supplementary Fig. 1), which were subsequently coated with high-reflectivity dielectric layers (Supplementary Information) ²⁰. The fiber mirrors were aligned and affixed laterally within a cut fused silica ferrule (Fig.1A, B) to increase the passive mechanical stability ⁴⁰. Optical modes were probed with static-frequency lasers over 660-760 nm while

monitoring reflection and transmission (Fig. 1A). The mirror separation was ~20 µm (Fig. 1B), leading to Q-factors of ~2×10⁶ and mode volumes of ~80 µm^{3 20}. Continuous probing of a single resonant mode was achieved via Pound – Drever – Hall (PDH) frequency locking ^{24,42}, in which the cavity length was actively stabilized to a single frequency of the pump laser (Fig. 1A). The input power into the cavity was ~5 μW resulting in a circulating power of 5.5 mW. We demonstrate the ability to detect single label-free molecules by introducing samples of varying mass (66-1.2 kDa) and radius (2.80-0.75 nm) into the FFPC. Protein samples were prepared at pM concentrations such that the mean occupancy of the optical mode volume was much less than one molecule. Intensity traces show high amplitude, correlated signals, manifesting as a negative peak in transmission and a positive peak in reflection from transient interactions between single diffusing protein molecules and the locked cavity mode (Fig. 2A), resulting in extraordinarily high SNRs of up to 123 for the 10 amino-acid peptide Myc-tag (Extended Data Fig. 1). Confirmation that signals originated from single-molecule diffusion was achieved by showing water background measurements before introduction of protein and after removal, during which no signal was observed (Supplementary Fig. 2); demonstrating that detected events increased linearly with protein concentration (Extended Data Fig. 2); and seeing Poisson statistics in arrival times (Extended Data Fig. 3). Without relying on plasmonic enhancement mechanisms ^{10–12,43}, surface proximity ^{3,10–14,43}, or the consequent conformational or chemical change of a surface-supported docking molecule ^{14,43}, we demonstrate SNRs of up to 42-fold higher than existing label-free biomolecule sensing techniques for molecules of comparable molecular weight (Supplementary Fig. 4) 3,10-14. Our approach also achieves a mass limit of detection ~25-fold smaller than that of direct mass photometry ⁷, and when compared to mass photometry with machine learning, achieves an ~8-fold smaller limit of detection while offering ~70× higher SNR 44. Though the data presented here is in pure water, proteins also give strong single-molecule signals in their more native phosphate-buffered saline (Extended Data Fig. 4). Each transit event comprises both temporal and intensity data. Most data were acquired

111

112

113114

115

116

117

118

119

120

121

122

123

124

125

126

127

128129

130

131

132

133134

135

136

137

138

139

140

141

142

143

144

145

146

147

Each transit event comprises both temporal and intensity data. Most data were acquired with a temporal resolution of 20 μs, but 2 μs time resolution (500 kHz acquisition rate, Extended Data Fig. 5) was also possible, suggesting the potential to capture even faster dynamics. Plotting the distribution of temporal and intensity parameters provides a 2D signal profile containing unique information on the molecular mass and diffusion (Fig. 2B). Each protein molecule exhibited a distribution of temporal widths, identified from the full width at half maximum (FWHM) of events that rise significantly above the noise, and prominences, which increased with increasing protein molecular weight (Fig. 2B). A diversity of widths is expected due to the stochasticity of Brownian motion. The downward shift to lower prominences at shorter transient times is due to a combination of this same diversity of molecular spatial paths and different intrinsic system response for smaller molecules. To

demonstrate the ability of this technique to move beyond detection, we explored the potential for property assay by calculating the autocorrelation function of time traces containing multiple individually-detected molecules to extract temporal information from the data. Correlation spectroscopy is a ubiquitous tool across temporally sensitive biophysical methods, such as fluorescence correlation spectroscopy (FCS) and dynamic light scattering, aiming to extract ensemble diffusional and, therefore, size and mass information of molecules 41,45-49. FCS typically suffers from significant Poisson noise due to the limited number of detected fluorescence photons per molecule, a particular problem in versions that rely on intrinsic fluorescence ⁵⁰. In contrast, our microcavity-based readout is based on >10¹² of detected photons per second, even facilitating faster sampling (Extended Data Fig. 5). Our method is also capable of quantifying diffusive behavior on molecules >50 times smaller than other label-free single-molecule methods ^{15,16}. The autocorrelation expectedly shows dynamics on longer timescales for proteins of increasing mass (Fig. 3A). Importantly, the autocorrelation times were consistently linear in proportion to the radius of the protein (Fig. 3B). This result confirms the versatility of this new single-molecule technique as a molecular property assay, demonstrating the potential to extract meaningful molecular information, including size and diffusional properties. Label-free methods of assessing molecular dynamics can offer substantial impact in biophysical applications.

Having demonstrated single-molecule measurements of solution-phase, label-free proteins, we next demonstrated the ability to resolve populations of simple binary mixtures. Resolution of mixtures is vital for identifying diagnostic biomarkers, understanding disease pathogenesis, and for elucidating biomolecule-biomolecule and biomolecule-drug interactions. Techniques such as FCS, invaluable for inferring conformation, and fluorescence polarization anisotropy, invaluable for ascertaining drug binding ⁵¹, are generally limited by the requirement for fluorescent labels. Ensemble label-free techniques such as dynamic light-scattering can provide diffusive information of biomolecules, but analysis is restricted by the high dependence of scattering on the molecular radius (r⁶), obscuring small particles among larger ones ⁵², necessitating monodisperse samples for quantitation⁷. Our approach produces 2D profiles that can act as molecular signatures (Fig. 2B) containing information about mass and diffusivity.

First, we investigated a mixture of aprotinin and Myc-tag, which have a 5.3 kDa mass and 0.7 nm radius difference (Fig. 4A). The contour plot of the mixture is qualitatively similar to the sum of the pure component distributions. Though these two populations would be difficult to resolve considering only peak prominence, two distinct populations, a fast-moving population with a mean event FWHM of 0.49 ± 0.15 ms and a broader, slow-moving

population with a mean event FWHM of 1.68 \pm 1.37 ms, are clearly evident in the 2D contour.

Moving beyond protein samples, we explored the resolution of bimolecular mixtures of DNA isomers of identical mass (16.6 kDa) and composition, but differing sequence (Fig. 4B, Extended Data Fig. 6, Supplementary Fig. 11): a DNA duplex (9 nm) and a Y-junction structure (5 nm). Here, the two populations are clearly resolved in the 2D contour plot and along either individual axis and both components are present throughout the experiment (Extended Data Fig. 7). Spiking in known pure DNA samples identified the larger prominence population as coming from the Y-junction (Extended Data Fig. 6). A ternary mixture of three DNA Y-junctions of differing mass was also measured (Supplementary Fig. 12) and found to be at the limit of resolvability and is further discussed in the Supplementary Information. As discussed below, the response of the FFPC to the molecular perturbation is influenced by molecular properties as well as multiple dynamic cavity properties. The ability to cleanly reveal the presence of two molecules of identical small mass but differing conformation and diffusion behavior shows that this approach provides complementary information that is not discernable from mass photometry.

Discussion

The detection of a single, freely moving, unlabeled small biomolecule with high SNR requires a plausible mechanism whereby the small perturbation to the optical system can be discerned. Our proposed mechanism begins with a refractive index change as the biomolecule displaces water molecules of lower index in the microcavity (often referred to as the "reactive mechanism") ³². Resonance shifts of 1-49 kHz due to the altered optical path length are estimated from the protein molecular weights (Supplementary Fig. 13). We note that these shifts are ~20× greater at equivalent weights than estimates in whispering gallery mode resonators ¹⁴ due to smaller mode volume and better spatial overlap between molecule and optical mode in FFPCs (Supplementary Information). The ability to resolve resonance shifts that are small compared to the cavity linewidth (~200 MHz) with such high SNR is based on a combination of high passive stability, active low-frequency stabilization, creation of a velocity discrimination window for molecular motion, and the use of dynamic photothermal distortion of the resonance line shape. In water, the photothermal effects occur due to absorption of some of the cavity circulating power, which alters the refractive index of the medium via the thermo-optic coefficient.

The combination of mounting the FFPC in a glass ferrule and PDH locking provides remarkable stability, suppressing mechanical and laser frequency noise to detector-limited levels (Fig. 5A, Supplementary Fig. 14) ⁴⁰. Importantly, the PDH locking bandwidth (LBW) only suppresses fluctuations (including molecular fluctuations) at temporal frequencies

below 5 kHz (Fig. 5A), where low-frequency mechanical fluctuations can introduce substantial resonance shifts. This loop would also suppress perturbations produced by larger, slow-moving molecules or particles, as the majority of their displacement would occur within the PDH LBW (Fig. 5A). Importantly, small molecules undergoing Brownian motion, albeit with smaller overall resonance shifts due to their reduced size, have a larger fraction of their mean squared displacement power spectral density (MSDPSD) 53 outside the PDH suppression window (Fig. 5A, Supplementary Fig. 15). Integration of the MSDPSD for the smallest protein (Myc-tag, 0.75 nm) between the end of the locking bandwidth and the photothermal bandwidth (discussed below) yields a root-mean-squared (RMS) displacement of 93 nm (supplementary materials). This displacement is comparable to the ~250 nm distance between the node and antinode of the cavity standing wave (Extended Data Fig. 8), suggesting that the near full resonance shift from the diffusing molecule can be experienced by the microcavity outside the PDH LBW. When the molecule diffuses back into the node, the perturbation ceases, leading the system to exhibit a dependence on the molecular diffusion constant (Fig. 3). Detection by shifting from node to antinode is distinct from the operational mechanisms in evanescent detection modalities 3,11,12,14,43. Critically, a solutionphase label-free apparatus allows this novel employment of PDH as a high-pass filter to reduce mechanical noise while passing signals from fast-moving molecules (Fig. 5B), a key difference compared to previous schemes.

240241

242

243

244

245246

247248

249250

251

252253

254

255

256

257

221

222

223

224

225

226

227

228

229

230

231

232

233

234

235

236237

238

239

The second element of our proposed mechanism relies on a photothermally induced distortion of the resonance line shape (Fig. 5C) and a dynamic photothermal priming mechanism, which amplifies small resonance shifts. FFPCs spatially confine relatively intense optical fields, inducing on-resonance temperature changes inside the mode volume media and consequent thermo-optic resonance shifts ²². The presence of this thermal nonlinearity clearly manifests as a broadened asymmetric cavity line shape upon active scanning of the cavity length or wavelength (Fig. Extended Data Fig. 9) ²³. This photothermal nonlinearity arises from the mirror coatings and the aqueous medium and requires no light absorption by the molecule itself ^{32,54}. The photothermal bandwidth was determined experimentally to be 21 kHz (Supplementary Fig. 16A), defining the upper limit of our molecular observation window (Fig. 5B). In a non-PDH stabilized cavity, these photothermal nonlinearities result in multiple distinct stable equilibria ²². However, with PDH stabilization, this nonlinearity can be used for additional signal amplification. Increasing the cavity transmission by introducing an offset from the original, arbitrary locked position (Fig. 5C, panel 1) results in the pump laser sitting at a frequency just lower than the cavity maximum (Fig. 5C, panel 2). In this primed state, even the resonance shift of a diffusing molecule can shift the cavity resonance to an unstable regime where the pump laser sits at a higher

frequency than the microcavity resonance (Fig. 5C, panel 3). Here, the shift triggers a dynamic process by which the cavity cools faster than the LBW, resulting in further resonance shift and more cooling, ultimately causing a substantial transmission decrease (Fig. 5C, panel 4). Other molecule-induced mechanisms, such as scattering, may also contribute to cavity cooling. After the molecule has diffused out of the antinode, the cavity begins to warm, and eventually, the PDH recovers the initial locked position at a rate defined by the LBW (Fig. 5C, panel 2). In the case of smaller perturbations (as with Myc-tag), the cavity cools less, leading to the distribution of peak prominences. Evidence for this mechanism can be found in controlled voltage pulses added to the output servo of the PDH, providing internal perturbations that qualitatively mimic molecular passages (Extended Data Fig. 10).

In summary, our proposed mechanism features molecules diffusing into the microcavity, where their fast motion exceeds the PDH locking bandwidth. A hypersensitive photothermally primed cavity, experiencing these fast molecular perturbations, rapidly cools, leading to enhanced shift and massive signal. Both peak prominence and temporal width are expected to be influenced by system parameters, including PDH LBW. However, while peak prominence is a complex function of biomolecule molecular weight (and thus refractive index) and diffusive parameters, the temporal width is expected to be dominated more purely by diffusive parameters, leading to clear linear dependence (Fig. 3). Future work will allow more quantitative information to be derived from peak prominence.

279 Conclusion

In the absence of surfaces, extrinsic labels, and plasmonic enhancers, this work has demonstrated exceptional sensitivity in observing single, diffusing biomolecules, achieving SNRs of >100 for a sub 1 nm peptide. Our approach leverages the open-access geometry of micro-scale FFPCs to facilitate unimpeded biomolecule diffusion as well as maximize the overlap between the biomolecules and the optical field. Our enhanced sensitivity relative to other label-free techniques (Supplementary Fig. 4) originates in molecular velocity filtering and photothermal priming, where two experimental challenges, fast molecular motion, and thermal nonlinearity, are transformed into advantages. The resulting rich 2D intensity/temporal data can be used to distinguish unique, identifying molecular signatures and has the potential to provide quantitative mass and diffusional information.

Mass photometry, a new method that can provide quantitative mass information of unlabeled biomolecules⁷, has been commercialized and widely adopted, showcasing the tremendous possibilities of photonic single-molecule assays. Alternatively, our solution-phase FFPC-based approach avoids surfaces while providing µs-scale dynamics, a substantially higher sensitivity with ≤1 kDa detection limit, and 2D signal profiles that offer a path toward

distinguishing molecules based on conformation, which influences diffusion properties, as well as just mass. FFPCs offer convenient fiber optic integration and molecules, after passing through the FFPC, could be readily interrogated via mass photometry, making the approaches truly complementary. Our approach also brings certain limitations at its current level of maturity (Supplementary Information). The nonlinearity of the signal, originating in the interplay between optical and thermal dynamics, imposes difficulties on the ability to derive quantitative information from peak prominence and to resolve more complex mixtures. Spatial resolution, so valuable in interferometric scattering, is largely absent in our method. The need for pM-level sample concentrations will provide benefit in sample-limited applications but also impose constraints on the ability to study bimolecular interactions. Future work will ascertain which of these limitations are fundamental and which can be circumvented. Simple experimental advances, such as suppression of external noise sources, are expected to yield significant improvements, including the capability to detect biomolecules smaller than 1 kDa. Optimization of measurement parameters using a quantitative model will enable configuration of the bandwidth of the velocity filter to selectively collect information from different diffusional populations. Our FFPC approach has the potential to resolve rapid biomolecular conformation changes, elucidate self-assembly of small molecules in complex samples, and provide routes to rapid screening of proteinprotein and protein-drug interactions. By being label-free and single-molecule, our method can mitigate key experimental difficulties in FCS and dynamic light scattering, two widely applied biophysical techniques. This straightforward and readily scalable apparatus will bring numerous benefits to the fields of life and chemical sciences, such as trace analysis, separation science, mechanistic insights, and clinical diagnostics.

318319

295

296

297

298

299

300

301

302

303

304

305

306

307

308

309

310

311

312

313

314

315

316

317

References

- Moerner, W. E. Single-Molecule Spectroscopy, Imaging, and Photocontrol:
 Foundations for Super-Resolution Microscopy (Nobel Lecture). *Angewandte Chemie International Edition* 54, 8067–8093 (2015).
- Li, N. *et al.* Photonic resonator interferometric scattering microscopy. *Nat Commun* 12, 1744 (2021).
- Mauranyapin, N. P., Madsen, L. S., Taylor, M. A., Waleed, M. & Bowen, W. P.
 Evanescent single-molecule biosensing with quantum-limited precision. *Nat Photonics* 11, 477–481 (2017).
- 328 4. Piliarik, M. & Sandoghdar, V. Direct optical sensing of single unlabelled proteins and super-resolution imaging of their binding sites. *Nat Commun* **5**, 1–8 (2014).
- 330 5. Ortega Arroyo, J. *et al.* Label-free, all-optical detection, imaging, and tracking of a single protein. *Nano Lett* **14**, 2065–2070 (2014).

- 332 6. Taylor, R. W. & Sandoghdar, V. Interferometric Scattering Microscopy: Seeing Single
- Nanoparticles and Molecules via Rayleigh Scattering. Nano Lett 19, 4827–4835
- 334 (2019).
- 335 7. Young, G. *et al.* Quantitative mass imaging of single biological macromolecules.
- 336 Science **360**, 423–427 (2018).
- 337 8. Yu, D. et al. Whispering-gallery-mode sensors for biological and physical sensing.
- 338 Nature Reviews Methods Primers 1, 1–22 (2021).
- 339 9. Heylman, K. D. et al. Optical Microresonators for Sensing and Transduction: A
- Materials Perspective. *Advanced Materials* **29**, 1–29 (2017).
- 341 10. Zijlstra, P., Paulo, P. M. R. & Orrit, M. Optical detection of single non-absorbing
- molecules using the surface plasmon resonance of a gold nanorod. *Nat Nanotechnol*
- **7**, 379–382 (2012).
- 344 11. Baaske, M. D., Foreman, M. R. & Vollmer, F. Single-molecule nucleic acid
- interactions monitored on a label-free microcavity biosensor platform. *Nat*
- 346 Nanotechnol **9**, 933–939 (2014).
- 347 12. Dantham, V. R. et al. Label-free detection of single protein using a nanoplasmonic-
- 348 photonic hybrid microcavity. *Nano Lett* **13**, 3347–3351 (2013).
- 349 13. Yu, W., Jiang, W. C., Lin, Q. & Lu, T. Cavity optomechanical spring sensing of single
- 350 molecules. *Nat Commun* **7**, 12311 (2016).
- 351 14. Su, J., Goldberg, A. F. & Stoltz, B. M. Label-free detection of single nanoparticles and
- biological molecules using microtoroid optical resonators. *Light Sci Appl* **5**, 1–6
- 353 (2016).
- 354 15. Špačková, B. et al. Label-free nanofluidic scattering microscopy of size and mass of
- single diffusing molecules and nanoparticles. *Nat Methods* **19**, (2022).
- 356 16. Baaske, M. D., Asgari, N., Punj, D. & Orrit, M. Nanosecond time scale transient
- 357 optoplasmonic detection of single proteins. Sci Adv 8, 5576 (2022).
- 358 17. Wilson, H. & Wang, Q. ABEL-FRET: tether-free single-molecule FRET with
- 359 hydrodynamic profiling. *Nat Methods* **18**, 816–820 (2021).
- 360 18. Wang, Q., Goldsmith, R. H., Jiang, Y., Bockenhauer, S. D. & Moerner, W. E. Probing
- 361 Single Biomolecules in Solution Using the Anti-Brownian Electrokinetic (ABEL) Trap.
- 362 Acc Chem Res **45**, 1955–1964 (2012).
- 363 19. Vallance, C., Trichet, A. A. P., James, D., Dolan, P. R. & Smith, J. M. Open-access
- microcavities for chemical sensing. *Nanotechnology* **27**, 274003 (2016).
- 365 20. Hunger, D. et al. A fiber Fabry–Perot cavity with high finesse. New J Phys 12, 065038
- 366 (2010).

- 367 21. Kohler, L., Mader, M., Kern, C., Wegener, M. & Hunger, D. Tracking Brownian motion
- in three dimensions and characterization of individual nanoparticles using a fiber-
- based high-finesse microcavity. *Nat Commun* **12**, 1–7 (2021).
- 370 22. Carmon, T., Yang, L. & Vahala., K. J. Dynamical thermal behavior and thermal self-
- 371 stability of microcavities. *Opt Express* **12**, 4742–4750 (2004).
- 372 23. Brachmann, J. F. S., Kaupp, H., Hänsch, T. W. & Hunger, D. Photothermal effects in
- 373 ultra-precisely stabilized tunable microcavities. *Opt Express* **24**, 21205–21215 (2016).
- 374 24. Black, E. D. An introduction to Pound–Drever–Hall laser frequency stabilization. Am J
- 375 *Phys* **69**, 79–87 (2001).
- 376 25. Moerner, W. E. & Fromm, D. P. Methods of single-molecule fluorescence
- 377 spectroscopy and microscopy. Review of Scientific Instruments 74, 3597–3619
- 378 (2003).
- 379 26. Riback, J. A. et al. Commonly used FRET fluorophores promote collapse of an
- otherwise disordered protein. *Proceedings of the National Academy of Sciences* **116**,
- 381 8889–8894 (2019).
- 382 27. Zanetti-Domingues, L. C., Tynan, C. J., Rolfe, D. J., Clarke, D. T. & Martin-
- 383 Fernandez, M. Hydrophobic Fluorescent Probes Introduce Artifacts into Single
- 384 Molecule Tracking Experiments Due to Non-Specific Binding. *PLoS One* **8**, 74200
- 385 (2013).
- 386 28. Dietz, M. S., Wehrheim, S. S., Harwardt, M.-L. I. E., Niemann, H. H. & Heilemann, M.
- 387 Competitive Binding Study Revealing the Influence of Fluorophore Labels on
- 388 Biomolecular Interactions. *Nano Lett* **19**, 8245–8249 (2019).
- 389 29. Friedel, M., Baumketner, A. & Shea, J.-E. Effects of surface tethering on protein
- folding mechanisms. Proceedings of the National Academy of Sciences 103, 8396–
- 391 8401 (2006).
- 392 30. Wang, Q. & Moerner, W. E. Single-molecule motions enable direct visualization of
- biomolecular interactions in solution. *Nat Methods* **11**, 555–558 (2014).
- 394 31. Vahala, K. J. Optical microcavities. *Nature* **424**, 839–846 (2003).
- 395 32. Arnold, S., Shopova, S. I. & Holler, S. Whispering gallery mode bio-sensor for label-
- free detection of single molecules: thermo-optic vs. reactive mechanism. Opt Express
- **18**, 281–287 (2010).
- 398 33. Zhu, J. et al. On-chip single nanoparticle detection and sizing by mode splitting in an
- 399 ultrahigh-Q microresonator. *Nat Photonics* **4**, 46–49 (2010).
- 400 34. Foreman, M. R., Keng, D., Treasurer, E., Lopez, J. R. & Arnold, S. Whispering gallery
- 401 mode single nanoparticle detection and sizing: the validity of the dipole approximation.
- 402 Opt Lett **42**, 963 (2017).

- 403 35. Horak, E. H. et al. Exploring Electronic Structure and Order in Polymers via Single-
- 404 Particle Microresonator Spectroscopy. *Nano Lett* **18**, 1600–1607 (2018).
- 405 36. Heylman, K. D. *et al.* Optical microresonators as single-particle absorption
- 406 spectrometers. *Nat Photonics* **10**, 788–795 (2016).
- 407 37. Hümmer, T. et al. Cavity-enhanced Raman microscopy of individual carbon
- 408 nanotubes. *Nat Commun* **7**, 12155 (2016).
- 409 38. Hogan, L. T. et al. Toward Real-Time Monitoring and Control of Single Nanoparticle
- 410 Properties with a Microbubble Resonator Spectrometer. *ACS Nano* **13**, 12743–12757
- 411 (2019).
- 412 39. Trichet, A. A. P. et al. Nanoparticle Trapping and Characterization Using Open
- 413 Microcavities. *Nano Lett* **16**, 6172–6177 (2016).
- 414 40. Saavedra, C., Pandey, D., Alt, W., Pfeifer, H. & Meschede, D. Tunable fiber Fabry-
- 415 Perot cavities with high passive stability. *Opt Express* **29**, 974 (2021).
- 416 41. Haustein, E. & Schwille, P. Fluorescence Correlation Spectroscopy: Novel Variations
- of an Established Technique. Annu Rev Biophys Biomol Struct 36, 151–169 (2007).
- 418 42. Barnes, J. A., Gagliardi, G. & Loock, H.-P. Absolute absorption cross-section
- 419 measurement of a submonolayer film on a silica microresonator. *Optica* **1**, 75 (2014).
- 420 43. Baaske, M. D. & Vollmer, F. Optical observation of single atomic ions interacting with
- 421 plasmonic nanorods in aqueous solution. *Nat Photonics* **10**, 733–739 (2016).
- 422 44. Dahmardeh, M., Mirzaalian Dastjerdi, H., Mazal, H., Köstler, H. & Sandoghdar, V.
- Self-supervised machine learning pushes the sensitivity limit in label-free detection of
- 424 single proteins below 10 kDa. *Nat Methods* **20**, 442–447 (2023).
- 425 45. Torres, T. & Levitus, M. Measuring Conformational Dynamics: A New FCS-FRET
- 426 Approach. *J Phys Chem B* **111**, 7392–7400 (2007).
- 427 46. Kandula, H. N., Jee, A.-Y. & Granick, S. Robustness of FCS (Fluorescence
- 428 Correlation Spectroscopy) with Quenchers Present. J Phys Chem A 123, 10184–
- 429 10189 (2019).
- 430 47. Kratz, K., Hellweg, T. & Eimer, W. Structural changes in PNIPAM microgel particles
- 431 as seen by SANS, DLS, and EM techniques. *Polymer (Guildf)* **42**, 6631–6639 (2001).
- 432 48. Hoo, C. M., Starostin, N., West, P. & Mecartney, M. L. A comparison of atomic force
- 433 microscopy (AFM) and dynamic light scattering (DLS) methods to characterize
- nanoparticle size distributions. *Journal of Nanoparticle Research* **10**, 89–96 (2008).
- 435 49. Stetefeld, J., McKenna, S. A. & Patel, T. R. Dynamic light scattering: a practical guide
- and applications in biomedical sciences. *Biophys Rev* **8**, 409–427 (2016).
- 437 50. Roy, P., Claude, J. B., Tiwari, S., Barulin, A. & Wenger, J. Ultraviolet Nanophotonics
- 438 Enables Autofluorescence Correlation Spectroscopy on Label-Free Proteins with a
- 439 Single Tryptophan. Nano Lett 23, (2023).

- Jameson, D. M. & Ross, J. A. Fluorescence polarization/anisotropy in diagnostics and imaging. *Chem Rev* **110**, 2685–2708 (2010).
- 442 52. Bohren, C. F. & Huffman, D. R. Absorption and Scattering of Light by Small Particles.
- Absorption and Scattering of Light by Small Particles (Wiley, 1998).
- 444 doi:10.1002/9783527618156.

- Lukić, B. *et al.* Motion of a colloidal particle in an optical trap. *Phys Rev E Stat Nonlin*Soft Matter Phys **76**, 011112 (2007).
- 54. Gaiduk, A., Yorulmaz, M., Ruijgrok, P. V. & Orrit, M. Room-Temperature Detection of
 a Single Molecule's Absorption by Photothermal Contrast. *Science* 330, 353–356
 (2010).

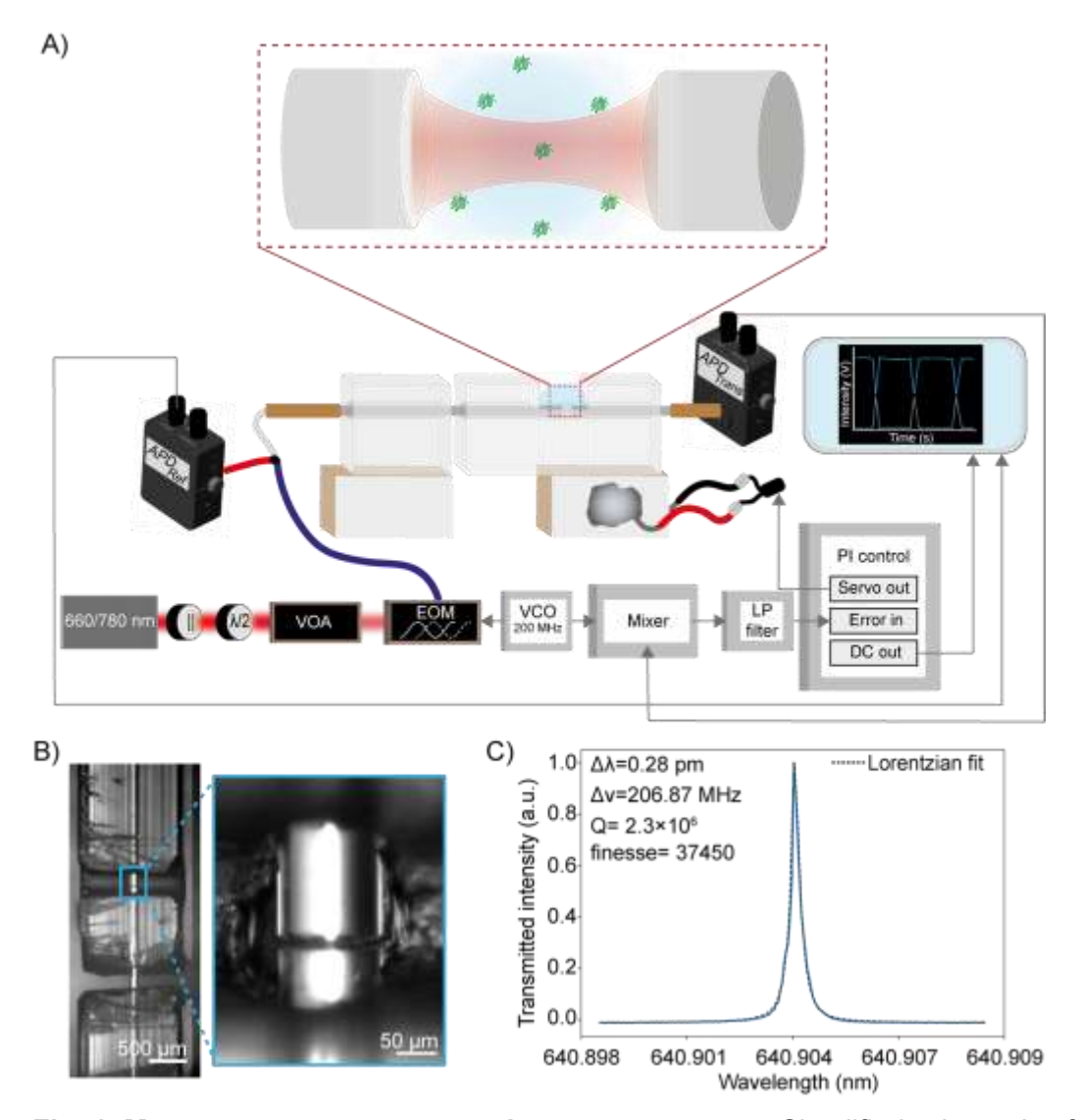


Fig. 1. Measurement apparatus and resonance scan. a Simplified schematic of the FFPC-based single-molecule sensing instrumentation. Laser light (660-760 nm) of <1 MHz spectral width was transmitted through a linear polarizer (||) and half-wave plate (λ/2), selectively attenuated with a variable optical attenuator (VOA), and phase-modulated through a lithium niobate electro-optic modulator (EOM) driven by a 200 MHz voltage-controlled oscillator (VCO). Light was then coupled into the cavity via a fiber splitter, to enable collection of reflected light, and into an input optical fiber with transmitted intensity detected on a photodiode. PDH cavity-length stabilization, to maintain the cavity on resonance with the laser, was achieved using the frequency sidebands generated by the EOM driven by the VCO at 200 MHz. The error signal was generated by applying a low-pass filter to the mixed VCO reference and photodiode signals. This signal was then fed into the proportional-integral (PI) controller, which drives the ceramic piezo actuators to stabilize the cavity length to maintain resonance. Protein diffusion events were monitored in two channels on separate photodiodes, reflection and transmission. b Brightfield images of the FFPC optical fibers within the quartz ferrule. The fibers were affixed within the ferrule, forming a

cavity 19.3 µm in length. **c** Wavelength scan used to determine the spectral linewidth of the cavity modes to be probed. The cavity finesse was 37450 in water.

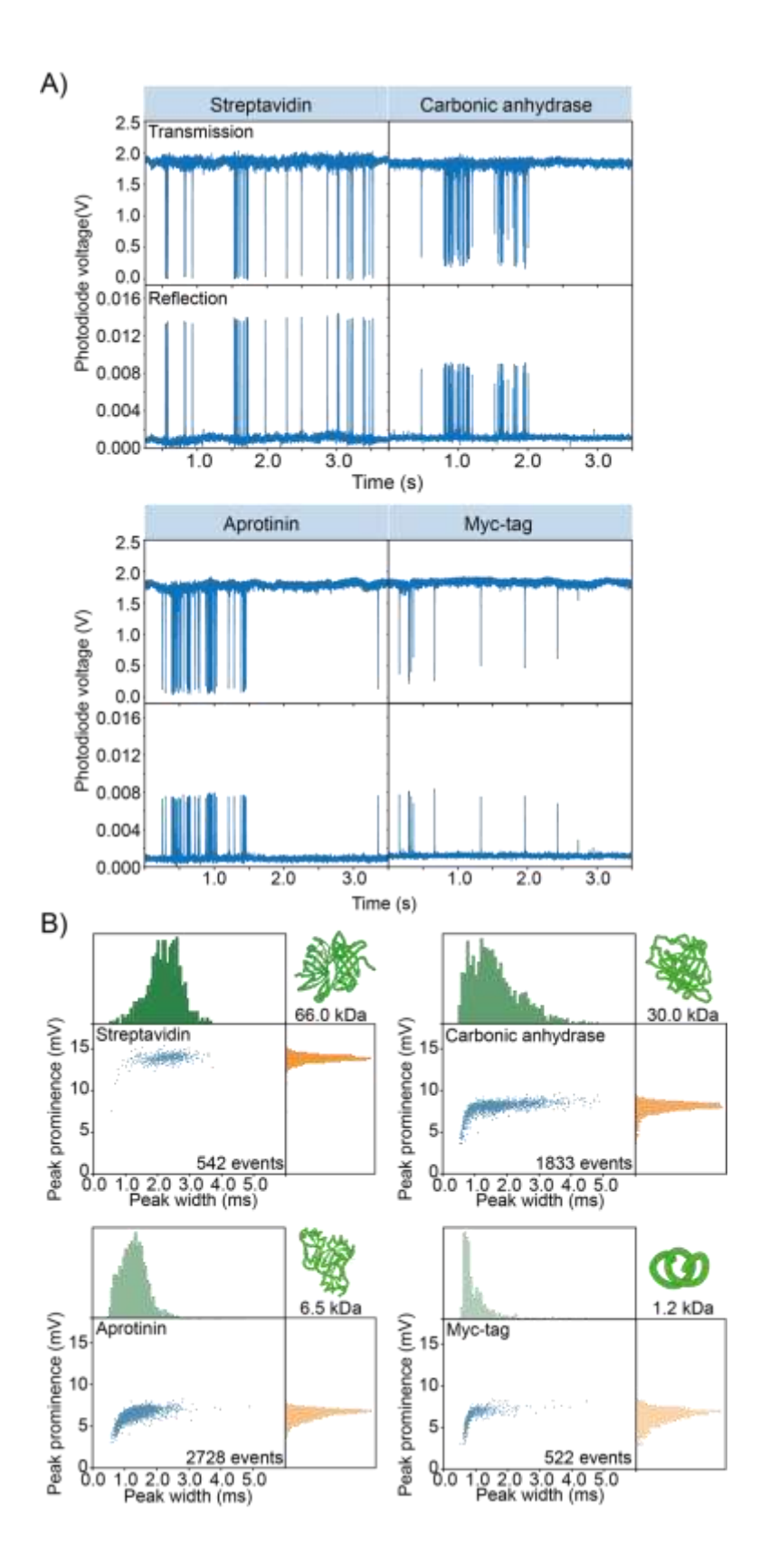


Fig. 2. Signals from individual molecules. a Perturbations of the locked resonant cavity mode originating from single-protein diffusion events. The locked signal was monitored in both transmission and reflection, and the events manifested as a transient reduction of the transmitted signal intensity and an increase in the reflected intensity. **b** 2D plots and

- 477 accompanied histograms of the extracted prominences and temporal widths of the reflected
- signals. The corresponding transmission data can be found in Supplementary Fig. 5.

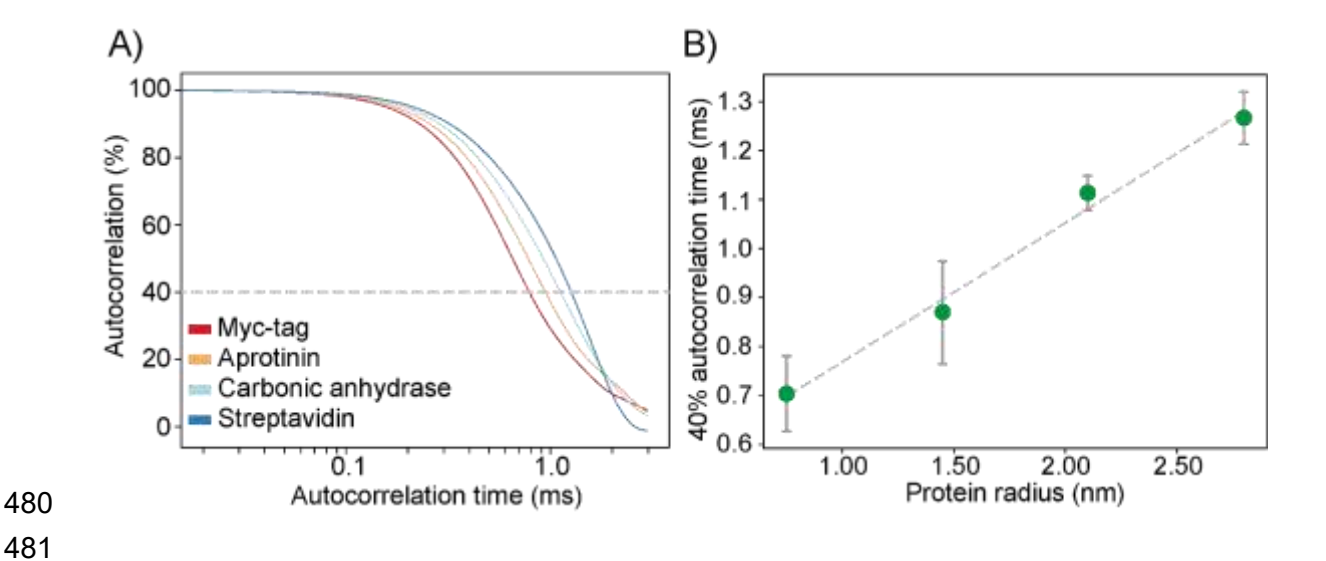


Fig. 3. Diffusion information from single-molecule profiles. a Ensemble autocorrelation of several hundred single-protein diffusion events. **b** Relationship between mean autocorrelation time at an autocorrelation threshold of 40% (see Supplementary Fig. 9 for other thresholds) and the protein radius, showing a clear linear correlation. The linear regression does not intercept the origin (Supplementary Fig. 10), likely due to the finite length of the instrument response function. The error bars represent the standard error of the mean from multiple experiments within the same cavity.

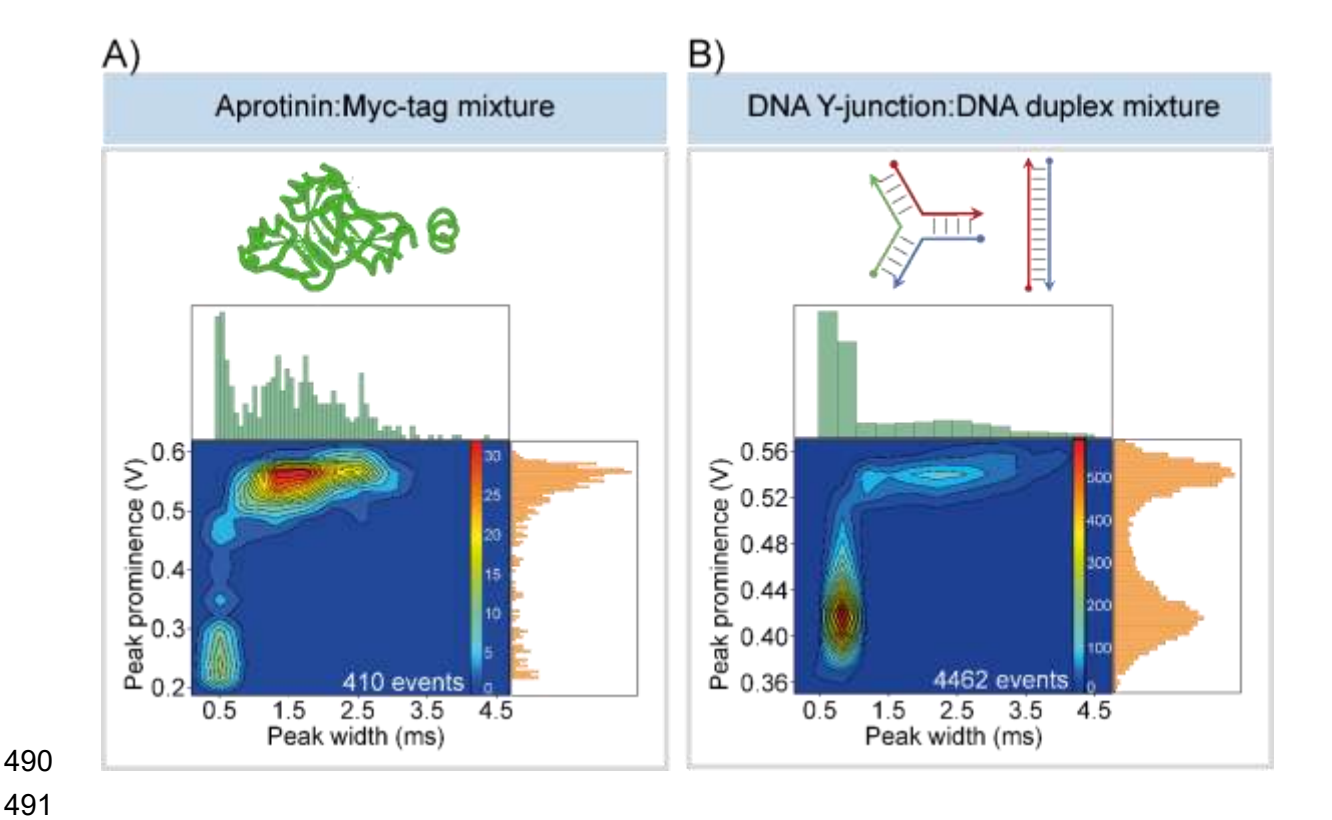


Fig. 4. Resolution of mixtures. Contour plots of peak prominence versus temporal width and subsequent independent histograms for **a** a mixed protein sample of aprotinin (6.5 kDa, 1.45 nm) and Myc-tag (1.2 kDa, 0.75 nm) and **b** a mixed DNA structure sample of a duplex (16.6 kDa, 9 nm) and Y-junction (16.6 kDa, 5 nm), with multiple populations clearly resolved.

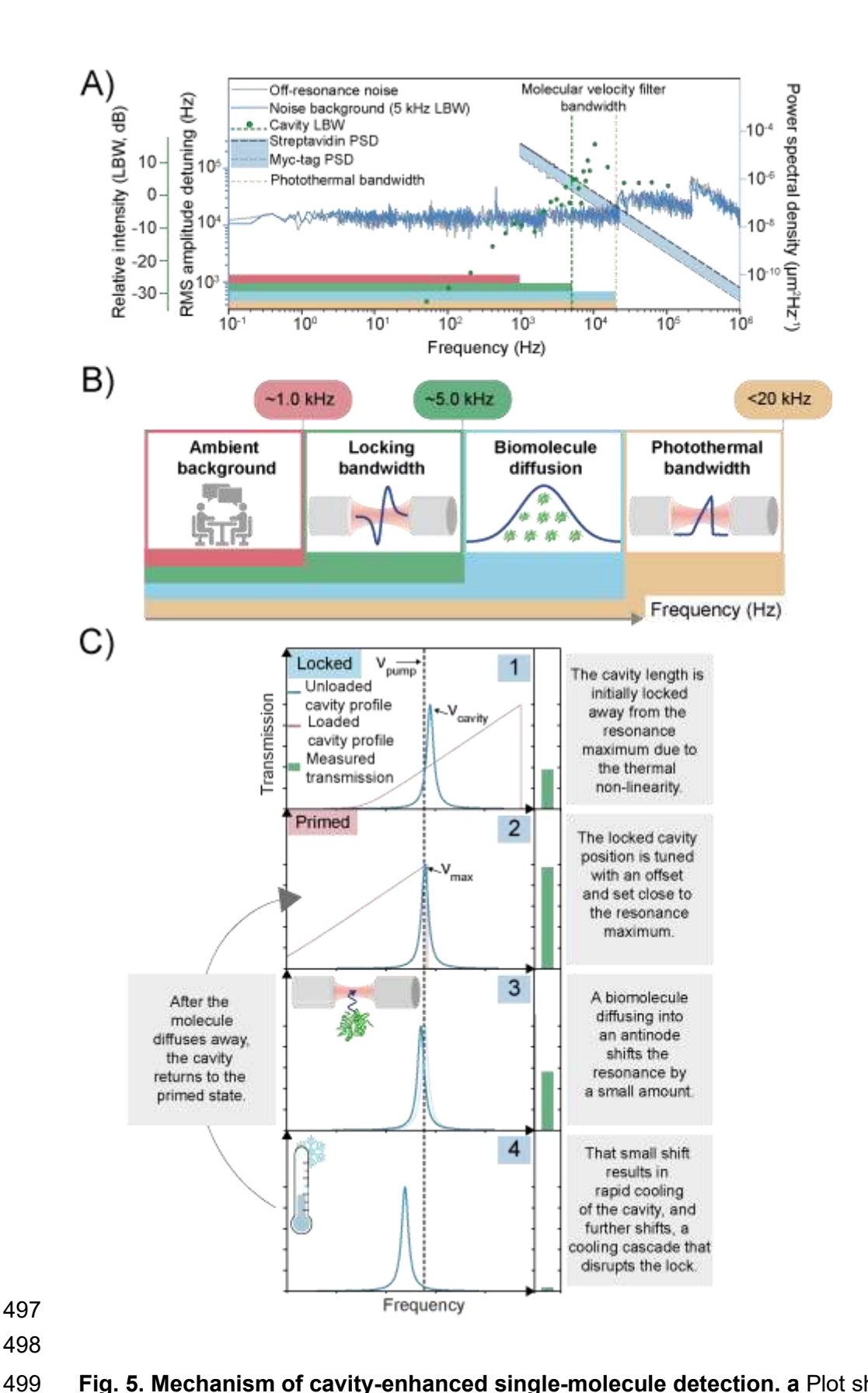


Fig. 5. Mechanism of cavity-enhanced single-molecule detection. a Plot showing frequency noise spectral density in water, LBW characterization, and mean-square-displacement power spectral density (MSDPSD) of proteins, streptavidin, aprotinin, carbonic

anhydrase, and Myc-tag. The noise spectral density of the locked cavity in water rapidly converges to the detector-limited noise (off-resonance noise), highlighting the high passive stability. The locking bandwidth of 5 kHz, defined by the 0 dB feedback gain crossing, governs the lower frequency limit of the velocity filter. The upper limit of the velocity filter is defined by the photothermal bandwidth (21 kHz). The molecular MSDPSD can be integrated within this filter bandwidth to determine the root-mean-square MSD **b** Cartoon illustrating the key processes and their frequency bandwidths. Noise below 5 kHz is suppressed by the PDH. The upper limit, defined by the LBW and the lower limit, defined by the photothermal bandwidth, determine the molecular diffusion velocity observation window. **C**) Schematic describing the mechanism of dynamic thermal priming (see text for details).

Methods

Mirrored fiber production

Copper-coated optical fiber with cladding diameter of 125 µm (IVG Fiber, Cu600) was first etched using nitric acid (70%). This etching procedure removed the copper coating, leaving a layer of carbon coating above the cladding. The carbon coating was removed with a small amount of diamond paste on cloth; however, this step was removed for later fiber production due to apparent contamination from the diamond paste. Fibers were flat-cleaved (<0.2-1°) using an automated cleaver (AFL Fujikura, CT-106) ⁵⁵.

An 18 W CO₂ laser (Synrad, 48-1 KAM) generated the ablation laser beam, which was guided and modified with polarizing, phase retarding, and other associated reflecting and ZnSe focusing optics. An arbitrary waveform generator (Agilent, 33220A) controlled the beam characteristics, and a digital optical power meter head (Thorlabs, S314C) with an attached console (Thorlabs, PM100D) was used to measure the beam power. Optical fiber substrates were mounted atop a fiber clamp (Thorlabs, HFF003), which rested upon a 3-axis translation system (Thorlabs, MTS50-Z8; MTS50B-Z8; MTS50C-Z8), driven by a DC servo motor controller (Thorlabs, KDC101) secured to a long-range single-axis translator for inspection-ablation positioning (Thorlabs, LNR502(/M)) driven by a motor controller (Thorlabs, BSC201). A CCD camera (Thorlabs, CS165MU) coupled to a long workingdistance microscope system (Navitar, 160-10) with a 20× magnification, 0.42 NA infinity corrected objective (Mitutoyo, 378-804-3) illuminated by a 635 nm LED source (Thorlabs, LEDD1B), was used to image the fiber position. Optimal ablation alignment was facilitated by illuminating the fiber core with an optical fault finder (VFLTOOL, HGB30). The laser was set to have a power of 0.28 W, and a shot time of 250 ms was controlled using a shutter in front of the fiber. These shot parameters generated fibers with radii of curvature (ROC) at the base of the ablation of 48 μm on average, and diameters, calculated by 2-σ of a Gaussian fit to the ablation profile, of 21 µm on average (Supplementary Fig. 1).

The fibers were characterized with a ZYGO Interferometer. Two perpendicular slices of the surface profile were analyzed. For calculating the ROC, the center of the ablation was assumed to be the minimum. A polynomial fit was then performed, and stepwise derivatives were averaged to calculate the ROC. For the diameter, Gaussian fitting was performed, and the diameter was taken to be two standard deviations of the fit. The ellipticity of the ablation was calculated by comparing both the ROC and the diameter values for the perpendicular slices. The decentration of the ablation was also measured by coupling the fault finder through the core of the fiber, which was then compared to the center of the ablation. The decentration, ROC, diameter, and ellipticity were all used to determine the viability of a fiber.

The fiber substrates were coated commercially with wavelengths of maximum reflectivity at either 635 nm (LASEROPTIK GmbH, Germany) or 635 and 780 nm (LAYERTEC GmbH, Germany), in which alternating layers of Ta_2O_5 and SiO_2 were deposited using ion beam sputtering (IBS). These generated distributed Bragg reflector surfaces with transmission loss < 20 ppm, absorption loss < 10 ppm and scattering loss < 16 ppm.

Ferrule-assembly Preparation

The cavity bridge assembly was prepared using fused silica ferrules (VitroCom, 8×1.25×1.25 mm) with an inner bore of 131 µm, based on the procedure by Saavedra et al. ⁴⁰. The glass ferrule was cleaned using an air plasma cleaner (Harrick Plasma, PDC-001-HP) for 10 minutes. A thin layer of UV-curable glue (Dymax, 9037-F) was placed on two 150 V piezos (Thorlabs, PA4DG), which were aligned flat to the ferrule, ensuring that the direction of translation was aligned with the long axis of the ferrule. The glue was then cured using a UV light (Rolence Enterprise, Q6 UV). The assembly of ferrule and two piezos was then affixed to a glass block, which was approximately 20×7×3 mm in dimension. This assembly was then placed in an oven at 65-75 °C for 2-3 hours for additional curing of the glue. After this, wires were soldered onto the piezos. Two cuts were made in the ferrule in order to facilitate translation of the cavity length: one full-cut to separate the ferrule into two parts, maximizing the cavity length translation, and one half-cut to preserve fiber alignment along the inner bore. These cuts were made using diamond wire (Ø=125 µm) secured in a jeweler's saw. The full-cut was made off center and the half-cut was made close to the center of the ferrule to provide access to the cavity mode. After the full-cut, a small piece of wire was placed in the bore to alert when the cut had reached the bore. During the cutting process the glass dust was removed using canned air.

The ferrule was cleaned post-cutting by first running the ferrule under deionized water for 5 minutes. Using a digital microscope to visualize, Millipore water was pipetted through the bore of the ferrule and a piece of optical fiber was run through the bore to remove any remaining glass dust. This process was repeated until no visible dust remained. The ferrule was then rinsed under Millipore water and few drops of methanol (≥ 99.9 %) were run through the ferrule, which was then dried thoroughly using a nitrogen gas line.

Fiber cavity construction

The previously described high reflectivity, mirror-coated optical fibers were spliced to a connectorized patch cable (Thorlabs, P3-630Y-FC-2) using a fusion splicer (Fujikura, FSM-100P). The fibers were aligned using a 6-axis piezo actuated stage (Thorlabs, MAX602D). The input fiber was mounted to this stage using a tapered v-groove fiber holder

(Thorlabs, HFV002). The output fiber was held by a v-groove fiber holder secured to an XYZ translation stage. To visually align the fibers, two cameras were aligned perpendicular to the fiber axis. The top-down view used a CMOS camera (Thorlabs, DCC1545M) connected to a zoom lens (Navitar, 1-50487). This imaging system was used for both alignment and to estimate the distance between the fibers. The second perpendicular axis was visualized using a digital microscope (Dino-Lite, AM4113ZT). Using both camera axes, the fibers were then coarsely aligned to one another visually using the 6-axis stage. The next step was to finely align the fibers by recording resonances. To do this, a ramp signal from a data acquisition board (DAQ, NI, BNC-2120) was applied to a piezo controller (Thorlabs, MDT693B), which drove the piezo aligned with the fiber axis. Laser light (635-760 nm) was then injected into the input fiber and collected through the output fiber to an avalanche photodiode (APD, Thorlabs, APD430A). Resonances were measured in transmission and optimized by adjusting all parameters of the 6-axis stage. The cavity finesse was characterized by either using a wavelength-tunable external cavity diode laser (Newport, TLB-6704) or via an electro-optic phase-modulator (EOM, EOSpace, PM-0S5-10-PFA-PFA-633, PM-0S5-01-PFA-PFA-765/781) by introducing sidebands at a known frequency (2.6 GHz) and the linewidth extracted via Lorentzian fitting. The mirror separation was ~20 µm (Fig. 1B), leading to Q-factors of ~2×10⁶ and mode volumes of ~80 μm³. The cavity finesses ranged from 27,000-101,000 across multiple cavities (Supplementary Information) in ambient conditions, reducing to 17,000-37,450 in water (due to increased absorption and scattering losses and the higher refractive index of the medium, Fig. 1C).

The fibers were guided into the prepared ferrule using the top-down and perpendicular views, and the cavity formed at the center of the half-cut. In order to secure the fibers inside the ferrule, 2 μ L of low-viscosity, UV-curable glue (Masterbond, UV16) was deposited onto each fiber in turn at the left entrance of the non-slotted ferrule and the right entrance of the slotted ferrule. The glue was drawn up the fiber using capillary action and was UV-cured (Rolence Enterprise, Q6 UV) after ~2 mm of travel into the ferrule. The piezos on the bridge were then attached to a piezo driver (nPoint, D.200) and driven to assess the resonances under constant cavity translation.

Optical setup

Experiments were performed on a custom-built setup (Supplementary Fig. 18). Either a single-frequency, continuous-wave diode laser (660 nm, Cobolt Flamenco, 90261, 300 mW) of < 1 MHz linewidth or a tunable Ti-Saph cavity laser of <100 kHz linewidth operating at a single frequency (760 or 780 nm, MSquared, SolsTiS) was passed through a linear polarizer and half wave-plate then fiber coupled into an electronic variable optical attenuator (Thorlabs, V600), then into an EOM (EOSpace, PM-0S5-10-PFA-633, PM-0S5-01-

PFA-PFA-765/781) driven by a voltage-controlled oscillator (VCO, Mini-Circuits, ZX95-209-S+, 200 MHz). The light was then coupled into the input fiber of the cavity via a fiber-based beam splitter (Thorlabs, TW670R3A1), the power injected into the cavity was between 5-35 μ W. The circulating power (P_{circ}) was calculated using Equation 1:

$$P_{circ} = P_{in}T\eta\left(\frac{F^2}{\pi^2}\right)$$
 Equation 1
$$\eta = \left|\left\langle\psi_{cav}|\psi_f\right\rangle\right|^2 \approx \frac{4d_m^2d_f^2}{\left(d_m^2 + d_\ell^2\right)^2}$$

where P_{in} is the input power 56 , η is the mode matching overlap integral 56 , $d_m=\omega(z=L/2)$ is the mode radius at fiber mirror (see eq. 10), d_f is the radius of the mode inside the SM fiber. T is the transmission factor of the mirror coating (transmission=10 ppm) and F is the cavity finesse. This expression is valid for all cavity systems influenced by absorption losses ⁵⁷. The remaining path of the splitter was collimated and then focused (Thorlabs, C560TME-B) onto the active area of an APD (Thorlabs, APD430A) enabling collection of reflected resonance light. The reflected signal voltage was sent to a DAQ board (NI, BNC-2120) and monitored using custom software. The transmitted light was collected through the output fiber of the cavity, collimated and focused (Thorlabs, C560TME-B) onto the active area of an APD (Thorlabs, APD430A). The transmitted signal voltage was sent to a diplexer (Mini-Circuits, ZDPLX-2150-S+), the low-frequency component (DC-10 MHz) was then directed to the DAQ board (NI, BNC-2120) in order to monitor the transmitted signal. The highfrequency component (50-2150 MHz) was amplified and sent to a frequency mixer (Mini-Circuits, ZP-1MH-S+) in which it was multiplied by the sinusoidal signal of the VCO under a homodyne detection scheme. The resulting frequency components were low-pass filtered (Mini-Circuits, SLP-1.9+) to extract the DC error-signal and directed to the error input of the Pound – Drever – Hall lockbox (PDH, Vescent, D2-125). The locking feedback was supplied to the piezos driving the cavity length via the servo output of the PDH lockbox.

Hardware control and data collection software

Experiments were performed using code written in-lab using Python 3 to handle both instrument control and data collection. The code interfaced with a DAQ board (NI, BNC-2120) and oscilloscope (Rigol, DS1104). For DAQ and oscilloscope connections, control was established using the PyLabLib package published under the GPL-3.0 license (doi.org/10.5281/zenodo.7324876). The control code was written together with a graphical user interface (GUI) to streamline user control. The GUI and interactable elements of the program use the Qt framework through PySide2 bindings under the GPLv2 license. A copy of the control software is available for free use under the GPLv3 license at https://github.com/FairhallAlex/ces_tools.

Sample preparation

657658

659 660

661

662

663

664

665

666

667

668

669

670

671

672

673

674

675

676

677

678

679

680

Protein samples included tetrameric streptavidin (66 kDa, 2.80 nm) ⁵⁸, carbonic anhydrase (30 kDa, 2.10 nm) ⁵⁹, aprotinin (6.5 kDa, 1.45 nm) ⁶⁰ and c-Myc peptide, known more commonly as Myc-tag (1.2 kDa, 0.75 nm) ⁶¹. Lyophilized Streptavidin (MilliporeSigma, 189730), Carbonic anhydrase (MP Biomedicals, 0215387910), Aprotinin (MilliporeSigma, A6106) and c-Myc peptide (MilliporeSigma, M2435) were dissolved to 1 mgml⁻¹ in phosphate buffered saline (pH 7.4), aliquoted to appropriate volumes and stored at -20 °C. For experimentation, samples were thawed on ice and diluted to the working concentration (0.25 pM-15 pM) in filtered (Ø= 20 nm, Whatman Anotop, WHA68091002) ultrapure Millipore water (18 M Ω , pH 7). To ensure that the measurements would be at the single-molecule level, the optical mode volume was calculated to host an average of 0.7 molecules at the highest working concentration (15 pM). DNA sequences for each construct were manually designed and validated by NUPACK (www.nupack.org). Commercially available oligonucleotides (Integrated DNA Technologies, Error! Reference source not found.) were purchased and used without purification. To assemble each structure, corresponding DNA strands (5 µM) were mixed in folding buffer (25 mM HEPES, 100 mM KCl, 10 mM MgCl2, pH 7.4), then annealed in a PCR thermocycler (Bio-Rad) by a linear cooling step from 95°C to 20°C over 2 hours (-0.1°C per 10 second). The products were further purified by a size-exclusion chromatography column (Superdex 200 increase 10/300) on a ÄKTA pure system (Cytiva), to remove extra strand and potential aggregates. The final concentration of each construct was determined by Nanodrop (Thermo Fisher Scientific). Samples were stored at 4°C for less than 1 month before use.

681 682

683

684

685

686

687

688

689

690

691

692

693

Single-Molecule Diffusion Experiments

Prior to introducing proteins, filtered (\emptyset = 20 nm, Whatman Anotop, WHA68091002) MilliQ water (8 µL) was added to the cavity. The input power in the cavity was controlled with an applied voltage to the VOA (Thorlabs, V600A) to ensure consistent power was used for all comparable experiments. The fundamental transmitted cavity mode was found under active cavity length translation and PDH-locked with a proportional gain of -40 dB. The locked position was tuned to the maximum possible transmission using the relative voltage offset on the lockbox (Vescent, D2-125). If spurious events were detected during the lock, the cavity was unlocked and cleaned under a flow of filtered MilliQ water and dried with N₂. This process was repeated after protein experiments to ensure the cavity was clean. The transmitted and reflected signals were monitored as a function of time at either 50 kHz or 500 kHz acquisition frequency. Intensity-time traces containing single-molecule events were

saved as .csv files every 30 seconds using the custom software described above. Water control experiments were continued until 5 minutes of data in the absence of a spurious signal was collected.

Solutions of proteins (either Streptavidin, Carbonic Anhydrase, Aprotinin, or Myc-tag, 0.2-15 pM, 8 μ L) or DNA (8 μ L, 10 pM) in filtered MilliQ water were introduced into the cavity. The input power in the cavity was controlled with an applied voltage to the VOA to ensure consistent power was used for all comparable experiments. The fundamental cavity mode was found under active cavity length translation and PDH-locked with a proportional gain of -40 dB. The transmitted and reflected signals were monitored as a function of time at either 50 kHz or 500 kHz acquisition frequency. Intensity-time traces containing single-molecule events were saved as .csv files every 30 seconds using the custom software described above. It is important to ensure that the single-molecule signals in the transmission geometry do not reach the noise floor of the detector as this will limit the achievable dynamic range when studying molecules of varying mass/size. This can be controlled by appropriately minimizing the input power and the relative voltage offset of the PDH locking system.

To produce single-molecule traces in phosphate buffered saline (Extended Data Fig. 4) (PBS, 10 mM phosphate, 150 mM NaCl, pH 7.4), the PBS was filtered through protein concentrators (ThermoFisher, 88152) using a centrifuge (Eppendorf, Minispin) at 12000 rpm for 30 minutes. The buffer filtered through the column was collected and additionally filtered (Ø= 20 nm, Whatman Anotop, WHA68091002). This cleaned buffer was then used to dilute aprotinin to a concentration of 15 pM. These experiments were conducted on a PDH-locked cavity in the same general manner as experiments in water. First, the cavity was cleaned with water until no spurious events were detected in water. Then cleaned buffer was added, again assuring no spurious events were detected. The aprotinin in PBS was then added to the cavity, and data was collected. After this step, the cavity was cleaned with water. Buffer control experiments under the same conditions were taken after the aprotinin experiments in the cleaned microcavity to ensure the signal collected previously was due to single-molecule diffusion events of the desired analyte (aprotinin).

Mixture experiments were conducted on a locked cavity in the same general manner as the single biomolecule diffusion experiments. Experiments began by adding filtered (\emptyset = 20 nm, Whatman Anotop, WHA68091002) MilliQ water (8 μ L) and cleaning the cavity with filtered MilliQ water, until 5 blank 30 second, consecutive transmission time traces could be obtained. This same process was repeated after the set of DNA experiments to ensure the cavity was clean and proper control data obtained.

DNA isomer spike experiments (Extended Data Fig. 6) were performed using a two DNA isomers (**Error! Reference source not found.**): a duplex (16.6 kDa, 9 nm) and a Y-junction (16.6 kDa, 9 nm). The duplex was diluted into filtered MilliQ water to a concentration of 1 pM and the Y-junction to a concentration of 20 pM. Equal parts of these solutions were then mixed for the initial mixture, yielding a concentration of 0.5 pM for the duplex and 10 pM for the Y-junction.

After the proper blank controls were obtained, the initial mixture (8 μ L) was added to the cavity. The cavity was then locked and data collected. After sufficient data was collected for this condition, the cavity was unlocked, approximately 6 μ L of solution were removed from the cavity, leaving solution behind, and the DNA duplex solution (6 μ L, 1 pM) were added to the cavity. This addition defines the first "spike." The cavity was then relocked, and data was taken for this next condition. Upon finishing data collection for the second condition, the cavity was again unlocked and 6 μ L of solution were removed from the cavity, and the DNA Y-junction (6 μ L, 20 pM) were added to the cavity. This was the second "spike" to the cavity. The cavity was relocked and data collected for this third condition. Importantly, at each step where solution is removed from the cavity, there is still solution from the prior condition remaining.

DNA ternary mixture spike experiments (Supplementary Fig. 12) were performed using three DNA Y junctions of varying mass: 9.2 kDa (2 nm), 16.6 kDa (4.5 nm), and 33 kDa (9 nm) (**Error! Reference source not found.**). The complexes were each diluted to 10 pM using filtered MilliQ water and then mixed in equal parts. This yielded an initial mixture of each species having a concentration of 3.3 pM.

After the proper blank controls were obtained, 8 μ L of the initial mixture was added to the cavity. The cavity was then locked, and data collected. After sufficient data was collected for this condition, the cavity was unlocked, approximately 6 μ L of solution were removed from the cavity, leaving solution behind, and 6 μ L of the 9.2 kDa complex (3.3 pM) were added to the cavity. This addition defines the first "spike". The cavity was then relocked, and data was taken for this next condition. Upon finishing data collection for the second condition, the cavity was again unlocked and 6 μ L of solution were removed from the cavity the 16.6 kDa complex (6 μ L, 3.3 pM) was added to the cavity. This was the second "spike" to the cavity. The cavity was relocked and data collected for this third condition. For the final condition, the cavity was unlocked and 6 μ L of solution were removed from the cavity and the 33 kDa complex (6 μ L, 3.3 pM) was added to the cavity. This is the third "spike" to the cavity and final condition, where the cavity was locked and data collected. Importantly, at

each step where solution is removed from the cavity, there is still solution from the prior condition remaining.

Signal Strengths and Temporal Samplings

The prominence of the peaks differed between transmission and reflection detection channels (Fig. 2B, Extended Data Fig. 1, Supplementary Fig. 5); this behavior arises from the dispersion that is unique to FFPC cavities (Supplementary Fig. 6) ⁵⁶. The mean temporal widths of the events were unchanged at proportional gain values > -50 dB in the proportional-integral (PI) control of the PDH system (Supplementary Fig. 7), where a higher proportional gain value constitutes a higher locking bandwidth (LBW). Consequently, experiments were conducted above this threshold at a LBW of ~5 kHz (Supplementary Fig. 8). Taken together, these data further confirm that these high amplitude signals originate from the perturbation of the cavity mode volume by single diffusing proteins.

The extraordinarily high SNR of the single protein events, even down to the 10 amino-acid peptide Myc-tag, highlights the potential to extend the dynamic range of applications to both smaller molecules and higher acquisition rates. To demonstrate this, we measured transient events of Myc-tag diffusion with 2 µs time resolution (500 kHz acquisition rate, Extended Data Fig. 5). This high collection frequency facilitated the measurement of events as narrow as 26 µs. With a 500 kHz collection frequency, even these high-speed events can be sampled far beyond the minimum Nyquist requirement, highlighting the potential to study kHz processes such as enzyme kinetics and conformational changes ⁶² without sacrificing SNR. Potentially higher sampling rates can be achieved with minimum contribution of photon shot noise using faster analog electronics, as demonstrated recently, ¹⁶ but the finite photothermal bandwidth (see below) may limit the sensitivity at highly elevated sample rates.

Locking bandwidth characterization

The locking bandwidth (LBW) of the cavity was measured by adding a harmonic perturbation (F_h) of known frequency and amplitude together with the error signal (e) using a voltage adder to the PI input (Supplementary Fig. 17). To maintain a linear relationship between the voltage of the error signal during locking and the frequency detuning of the cavity, we optimized the amplitude of the perturbation to 0.2×10^{-5} the peak-to-peak amplitude of the error signal. While the cavity was locked, we registered the sum of the perturbation signal and the error signal for different frequencies of the perturbation signal. This allowed us to measure the frequency at which the lock ceases to be effective at compensating for the perturbation to the system to determine the 0 dB gain value and thus the LBW of ~5 kHz (Supplementary Fig. 8, Figure 5A).

Noise floor determination

We measured the noise profile of the locked cavity from the error signal data. The voltage amplitude of the error signal was converted to its corresponding cavity frequency shift using the scanned error signal slope calibrated with the modulation sidebands at 2.6 GHz. From the calculated Fourier transform of the error signal, we extracted the RMS values of the cavity resonance frequency shift. We performed this measurement for different proportional gain settings where the maximum noise suppression was reached for the maximum locking bandwidth at ~5 KHz. The noise floor was measured from the offresonance error signal. This value, as well as the cavity finesse and gain, determine the LBW. We found effective noise suppression of external perturbations by the PDH-locking loop at the level of the noise floor throughout the LBW. While the source of low frequency noise is mainly due to ambient acoustic waves, mechanical waves that couple through the cavity system via contact points to the optical table, higher frequency noise (above the LBW) inherent to the electronic control systems is suppressed using a low pass passive filter before the piezo connection. Mechanical resonances of the cavity are expected to appear at frequencies above the LBW, however its magnitude is below the detector noise floor 40, at the level of 10³ HzHz^{-1/2} (Supplementary Fig. 14). The high mechanical passive stability of the cavity and the active PDH defines a frequency region where the cavity can be more sensitive to internal perturbations as described in the main text.

818 819

820

821

822

823

824

825

826

827

828

829

830

831

832

833

834

835

817

799

800

801

802

803

804

805

806

807

808

809

810

811

812

813

814

815 816

Voltage pulse experiments

To demonstrate the mechanism described in the main text (Figure 5C), we induced controlled perturbations to the locked cavity to mimic molecular perturbations to the cavity. The passage of molecules into the cavity results in an increase in the average refractive index, and a consequent decrease in frequency. This frequency decrease was mimicked by transiently, slightly increasing the length of the cavity by applying a voltage pulse to the piezo. Based on the measured duration of molecular transit events (Extended Data Fig. 1) and their prominence, we initially selected the parameters of the pulse, including duration and amplitude, to approximately induce similar detuning magnitudes and cavity transmission profiles (Extended Data Fig. 10). Square pulse signals of 140 µs-1 ms duration (Extended Data Fig. 10) and 1 Hz repetition rate were produced to affect the cavity length while the cavity was locked. The pulse produced by a function generator (Keysight, DSOX1204G) was added to the servo output of the lockbox; this combined signal was then directed to the piezos. The transmission signal of the locked cavity over time was recorded to ensure that all perturbation events and pulse signals were correlated (Extended Data Fig. 10A). A small reaction delay was seen due to the length of the cables that drive the piezo, the reaction time of the electromechanics and the transmission signal to the DAQ card. The transmission

profile (Extended Data Fig. 10, blue trace) is the result of the step up voltage perturbation (gray) which produced a steep reduction of the locked transmission signal due to the photothermal effect (a), this was followed by a brief recovery to the locked state by the PI feedback (b) followed by a second descent of the transmission signal as the step-up voltage of the pulse shifts the cavity in the opposite direction (c), finally the PI control recovers the locked state (d). When the pulse is generated, the resulting perturbation has a profile that resembles the transmitted signal profiles of the cavity due to the molecular interaction, (Figure 2A, Extended Data Fig. 1).

Photothermal broadening and thermo-optic coefficient

Optical microcavities with small mode volumes are susceptible to dynamic photothermal nonlinearities that originate from the build-up of intense optical fields, causing the temperature to increase in the cavity due to the absorption of this electromagnetic energy by the cavity constituents. Coupling between the heat and cavity resonance frequency can result in drift of resonance frequencies, and cooling cascades ²².

These photothermal dynamics depend on the thermo-optic coefficient (dn/dT) of the medium dominating the thermal dissipation. Increasing the temperature of a medium with a negative dn/dT will result in a decrease in the refractive index, and a consequently lower cavity resonance wavelength (high frequency). When the cavity length or laser frequency is scanned, the resonance may drift to higher or lower wavelengths depending on the direction of the scan and the cavity-laser detuning. When the cavity length is scanned to longer lengths, the optimal resonance condition (Equation 2),

 $m\lambda = 2nL$ Equation 2

where m is an integer, λ is the wavelength, n is the refractive index of the medium and L is the cavity length, appears to change as n decreases, resulting in a need for still higher lengths, and resulting in a distorted line shape, (Extended Data Fig. 9). This behavior is expected in FFPCs when the medium is air and the thermal dissipation is dominated by the mirror coatings, where an "effective" negative dn/dT^{23} due to thermal expansion results in a shorter cavity length ⁵⁶. A negative dn/dT is also expected when the medium is water ⁶³. We characterized the photothermal behavior in our FFPCs with water, by actively scanning the cavity to increasing length and observing the direction of photothermal broadening in water (Extended Data Fig. 9). A positive voltage gradient was applied to one of the piezos and confirmation that the positive voltage corresponded to increasing cavity length was achieved by tuning the wavelength of the pump laser and observing a shift of the resonance position to higher voltages with a lower pump wavelength. The direction of the broadened resonance

was observed to be towards longer cavity lengths, thus lower wavelengths, as expected for a system dominated by a medium with a negative thermo-optic coefficient.

Photothermal bandwidth measurement

Photothermal broadening of cavity lineshapes as a function of applied ramp speed were recorded in order to quantify the photothermal bandwidth of the cavity in water (Supplementary Fig. 16A). Resonances were recorded in transmission as a function of time and the cavity length was tuned using a ramp signal applied to the piezos from a function generator (Keysight, DSOX1204G). Phase modulated sidebands at a known frequency (2.6 GHz) were applied to be used as a frequency calibration marker to each trace. Initially, the ramp frequency and amplitude were chosen to minimize the photothermal effects in the cavity. This was determined by matching resonance lineshapes during both the increase and decrease of ramp voltage. This trace was used to measure the linewidth of the cavity. From there, the ramp speed was scanned and traces were recorded for both the increase and decrease in ramp voltage components of the ramp signal.

Data analysis for single-molecule diffusion and autocorrelation analyses

Analysis of transmitted and reflected signals resulting from perturbation by single biomolecules was performed with custom written code using Python 3. Raw data was passed through a low-pass filter (1.2 kHz) using the SciPy.signal butter package. Biomolecule and water control data collected at a single input power were first normalized to the maximum (for reflection) or minimum (for transmission) signal intensity to enable all signal peaks at a comparable power to be selected with a single threshold between 0-1. Single events were identified and analyzed using the SciPy.signal find_peaks package. Signal peaks were selected at a prominence threshold of 0.35. A temporal filter of 2 ms was applied to ensure that only peaks separated in time by greater than 2 ms were selected. Temporal widths were determined at the full width at half maximum of the event, and prominences were determined as the vertical distance between the maximum of the peak and the local background intensity.

Autocorrelation analysis was performed to quantify the temporal behavior of the single-molecule events in the intensity-time traces with custom code written in Python 3. A normalized function was generated by comparing time-shifted values to one another (Equation 3):

$$G_k = \frac{\sum_{i=1}^{N-k} (Y_i - \bar{Y})(Y_{i+k} - \bar{Y})}{\sum_{i=1}^{N-k} (Y_i - \bar{Y})^2}$$
 Equation 3

where k is the number of time steps, N is the total number of points, Y_i is the intensity for a specific time and \overline{Y} is the average intensity. Several 30 s intensity-time traces for proteins

diffusing in the locked cavity were concatenated. To ensure that the background was approximately continuous between files, the minimum of each file was found and then subtracted from every point. Events were identified with an intensity threshold 2.5 standard deviations from the mean and used to generate an autocorrelation trace. The function sm.tsa.acf from the package statsmodels.api, was used to generate the autocorrelation function. These functions were plotted for the four different proteins (streptavidin, carbonic anhydrase, aprotinin and Myc-tag, Figure 3A), and the values for different decay times were extracted. The time to decay to 40% of the autocorrelation time is shown to be linear with protein radius, Figure 3B. This linear trend was preserved for a large range of decay values (Supplementary Fig. 9), demonstrating the robustness of the analysis. A copy of the analysis software is available for free use under the GPLv3 license at https://github.com/FairhallAlex/ces_tools.

Data analysis for locking bandwidth determination

To extract the effective LBW of the system, the Fourier transform of the signal was measured at point S for each perturbation frequency (Supplementary Fig. 17). This Fourier analysis allowed us to decompose the signal into its frequency components, revealing how the system responds to different perturbation frequencies. The amplitudes at the perturbation frequencies were extracted and normalized with respect to the input signal F_h. This normalization process was crucial for comparing responses across different frequencies and conditions. The normalized amplitudes were then converted to decibels (dB) to provide a logarithmic scale that is commonly used in signal analysis. The result of the normalized values is shown as a function of input frequency of the sine wave (Figure 5A, Supplementary Fig. 8). The locking bandwidth was determined by identifying the frequency at which the normalized amplitude crosses 0 dB. This point represents the boundary where the locking system begins to lose its effectiveness in tracking and correcting for perturbations and was determined to be ~ 5 kHz. It is noteworthy that at higher frequencies, the signal exhibited amplification, attributed to a phase change in the control circuit referred to as the 'servo bump'. This phenomenon is accounted for in the analysis. Additionally, at even higher frequencies, the locking system had no discernible influence on the perturbation signal, resulting in a consistent relative intensity at 0 dB.

Signal-to-noise ratio determination

The data traces were smoothed using various bin sizes to generate a moving average, following:

$$F_{smoothed,i} = \frac{\sum_{j=i}^{i+(n-1)} F_{raw,j}}{n}$$
 Equation 4

where n is the bin size and F_i is the value of the function at index i. This smoothing procedure was performed for a series of different bin sizes from n=1 to n=250 (Supplementary Fig 18). Following smoothing, the trace was normalized. This process of smoothing the data was only performed for SNR calculations. To then calculate the signal-to-noise ratio (SNR), the standard deviation of the background (σ_N) was taken from the longest segment of background in the trace. The signal (S) was then calculated from the amplitude of the peaks and the SNRs for the proteins measured in this paper (Supplementary Fig. 4) were calculated by:

$$SNR = \frac{S}{\sigma_N}$$
 Equation 5

quantifying the SNR for each peak under each smoothing bin size. Giving the maximum average SNR, a bin size of 190 was used for all datasets. With a 50 kHz data acquisition rate and 190 point average, our SNR values can be considered to be over a 260 Hz bandwidth.

For comparison with other techniques, where provided, SNR values were taken directly from references 7,10,12,13,44 . For reference 3 , data was extracted into a .csv from Figure 4a using WebPlotDigitizer. The SNR was then calculated by taking the maximum of the signal and dividing it by the standard deviation of a region without signal. For reference 14 , the resonance shift was taken to be 5 am as a high estimate from Figure 5e and divided by the reported noise level of 9.6×10^{-4} fm. For reference 11 , the standard deviation of the noise was calculated by estimating 3σ from Figure 5b and dividing that by 3. The SNR was then calculated using the mean reported value of 2.5 fm for the 8-mer and then dividing by the previously calculated standard deviation.

Data analysis for photothermal bandwidth determination

To determine the photothermal bandwidth, the frequency shift of the photothermally broadened peak was calculated for each corresponding ramp speed. The photothermally broadened peak for each ramp speed had the larger distance between the left sideband and the main peak, which was determined to be the interpeak distance. Using this information, the frequency shift for each ramp speed was then calculated by calculating the difference between the photothermally broadened interpeak distance and the photothermally narrowed interpeak distance. The frequency shift as a function of the ramp speed (Extended Data Fig. 9) were then fitted to Equation 6 ²³.

$$\beta(x) = \frac{\beta_{ad}}{1 + x\tau}$$
 Equation 6

where β_{ad} and τ corresponded to the adiabatic thermal resonance shift and the thermal reaction time constant respectively. $\beta(x)$ is the number of linewidths shifted and x is the scan speed in linewidths/s. β_{ad} was calculated to be 8.28 linewidths and τ was calculated to be 23.7 microseconds. Then using Equation 7:

$$f_{th} = \frac{1}{2\tau}$$
 Equation 7

 τ was converted to f_{th} (21 kHz) which is the bandwidth for photothermal resonator length stabilization.

Data analysis for mixtures

In the main manuscript, Figure 4 demonstrates the resolution of mixtures of proteins and DNA isomers. This section discusses additional supporting experiments and further analysis of mixtures.

For the DNA mixture, the identity of each isomer in the mixture was confirmed by starting with a mixture (Figure 4B, Extended Data Fig. 6A), spiking in the Y-junction (Extended Data Fig. 6B), then spiking in the duplex (Extended Data Fig. 6C). Scatter plot versions of the contour plots in Figure 4 are shown in Supplementary Fig. 11. In a statistical mixture of molecules, there should be no extended time periods where only one population is observed, this is shown to be the case for both the protein and DNA mixtures (Extended Data Fig. 8). Any mode wandering in the microcavity can be identified by a sudden shift of a population to a different peak amplitude.

A 3-component DNA mixture of molecular weight 9.2 kDa, 16.6 kDa, and 33 kDa (Error! Reference source not found.) was studied, starting with the mixture (Supplementary Fig. 12A), and then independently spiking in each component. While the smallest (Supplementary Fig. 12B) and largest (Supplementary Fig. 12D) components are easily resolved (Supplementary Fig. 12ABCD), it is difficult to resolve the middle population (Supplementary Fig. 12C). When the middle population is spiked, a population is strengthened at (x,y)~(0.75 ms, 0.55 V). On the one hand, this population would not be visible looking at the one-dimensional histograms (green and yellow histograms), demonstrating the value of the 2D data. On the other hand, the location of this middle population on the 2D histogram appears to be highly sensitive to system parameters. Thus, resolving mixtures beyond binary mixtures appears to be at the edge of current feasibility. This problem is likely a result of the nonlinear nature of the readout and is further commented on in the "Error! Reference source not found." sections below.

Data availability

- 1005 A representative sample of the raw data supporting the findings of this work is openly
- available on figshare at [insert link here], under the title of [title of the dataset], with the
- 1007 following reference [ref/DOI]. The data is associated with Figures 2 and 3 in the main text.
- The sample data is in .csv format and available without restrictions.

- 1010 55. Brandstätter, B. *et al.* Integrated fiber-mirror ion trap for strong ion-cavity coupling.

 1011 *Review of Scientific Instruments* **84**, 123104 (2013).
- 1012 56. Gallego, J. *et al.* High-finesse fiber Fabry–Perot cavities: stabilization and mode matching analysis. *Applied Physics B* **122**, 47 (2016).
- 1014 57. Demtröder, W. Laser Spectroscopy 1. Laser Spectroscopy 1: Basic Principles
 1015 (Springer Berlin Heidelberg, Berlin, Heidelberg, 2014). doi:10.1007/978-3-642-538591016 9.
- Van Oss, C. J. *et al.* Macroscopic-scale surface properties of streptavidin and their
 influence on aspecific interactions between streptavidin and dissolved biopolymers.
 Colloids Surf B Biointerfaces 30, 25–36 (2003).
- Krishnamurthy, V. M. *et al.* Carbonic anhydrase as a model for biophysical and
 physical-organic studies of proteins and protein-ligand binding. *Chem Rev* 108, 946–
 1022 1051 (2008).
- 1023 60. Agić, D., Brkić, H., Kazazić, S., Tomić, A. & Abramić, M. Aprotinin interacts with substrate-binding site of human dipeptidyl peptidase III. *J Biomol Struct Dyn* **37**, 3596–3606 (2019).
- 1026 61. Evan, G. I., Lewis, G. K., Ramsay, G. & Michael Bishop, J. Isolation of monoclonal antibodies specific for human c-myc proto-oncogene product. *Mol Cell Biol* **5**, 3610–1028 3616 (1985).
- Hilvo, M. *et al.* Biochemical characterization of CA IX, one of the most active carbonic anhydrase isozymes. *Journal of Biological Chemistry* **283**, 27799–27809 (2008).
- Novais, S., Ferreira, M. S. & Pinto, J. L. Determination of thermo-optic coefficient of ethanol-water mixtures with optical fiber tip sensor. *Optical Fiber Technology* **45**, 276– 279 (2018).

1034

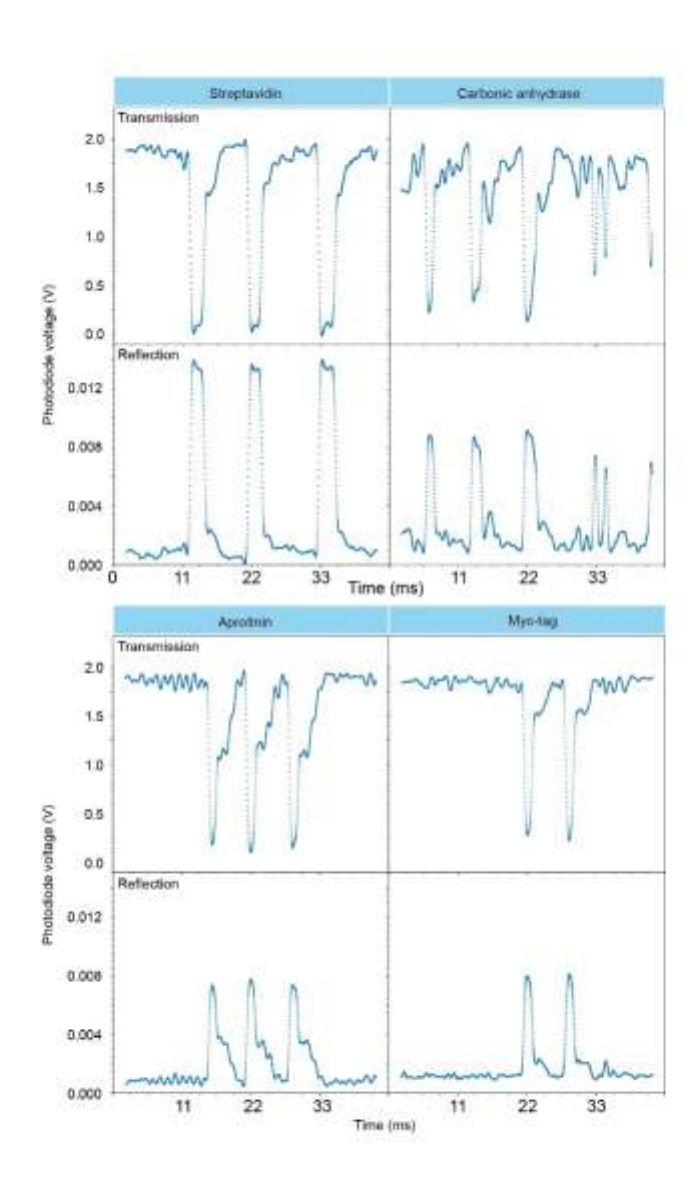
10351036

Acknowledgements

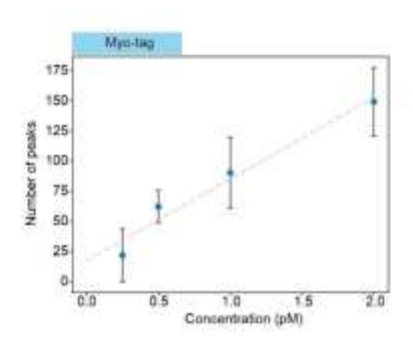
- This work was principally funded by the National Institute of Health (NIH, R01GM136981),
- with resonator construction supported by the Q-NEXT Quantum Center, a U.S. Department
- 1039 of Energy (DOE), Office of Science, National Quantum Information Science Research
- 1040 Center, under Award Number DE-FOA-0002253. Additional instrumentation development
- was supported by the Center for Molecular Quantum Transduction and the Energy Frontier

1042	Research Center funded by DOE, Office of Science, BES under award DE-SC0021314, the
1043	National Science Foundation (NSF) Quantum Leap Challenge Institute for Hybrid Quantum
1044	Architectures and Networks, Award No. 2016136, and by Schmidt Futures. LM. N. was
1045	partially funded by the European Union's Horizon 2020 research and innovation programme
1046	under the Marie Skłodowska-Curie grant agreement No 886216. E.C. was funded by NIH
1047	(MH061876 and NS097362). H.P. was funded by the Deutsche Forschungsgemeinschaft
1048	(DFG, German Research Foundation) under Germany's Excellence Strategy – Cluster of
1049	Excellence Matter and Light for Quantum Computing (ML4Q) EXC 2004/1 – 390534769. We
1050	thank D. Hunger, T. Northup, and S. Vanga for help in initial fiber mirror and microcavity
1051	fabrication, X. Huang and B. Cullinane for conversations on diffusion, M. Saffman for early
1052	conversations on fiber microcavities, and B. Thompson and T. Drier for instrumentation
1053	development.
1054	Author Contributions
1055	R.H.G. and LM.N. conceptualized experiments. B.S., Y. P., A.J.B., along with L.T.
1056	performed the CO ₂ fiber ablation with help from J.S., L.C.K., J.S.K., and H.P., LM.N.,
1057	J.K.R., and S.W. constructed the cavities with help from C.H.V LM.N. and J.K.R.
1058	performed single-protein experiments and protein data analysis. D.SB. performed
1059	autocorrelation analysis. J.K.R. and LM.N. performed protein and DNA mixture
1060	experiments. C.S. and R.H.G. devised experiments to confirm the mechanism. C.S., J.K.R.
1061	and LM.N. performed locking bandwidth experiments, noise characterization and
1062	photothermal bandwidth quantification. C.S. and D.SB. performed simulations. A.J.F. and
1063	B.M. wrote the hardware code. Z.Z. and E.R.C. designed and Z.Z. purified DNA constructs.
1064	R.H.G., LM.N., C.S., J.K.R. and D.SB. wrote the manuscript.
1065	
1066	
1067	Competing interests
1068	R.H.G. and LM. N. have submitted PCT/US2023/079347, "Methods And Systems For
1069	Detecting Diffusing Single Particles", filed November 10, 2023.
1070	
1071	Supplementary information
1072	The online version contains supplementary material available at
1073	
1074	Correspondence and requests for materials should be addressed to Randall Goldsmith.
1075	Reprints and permissions information is available at http://www.nature.com/reprints.
1076	
1077	

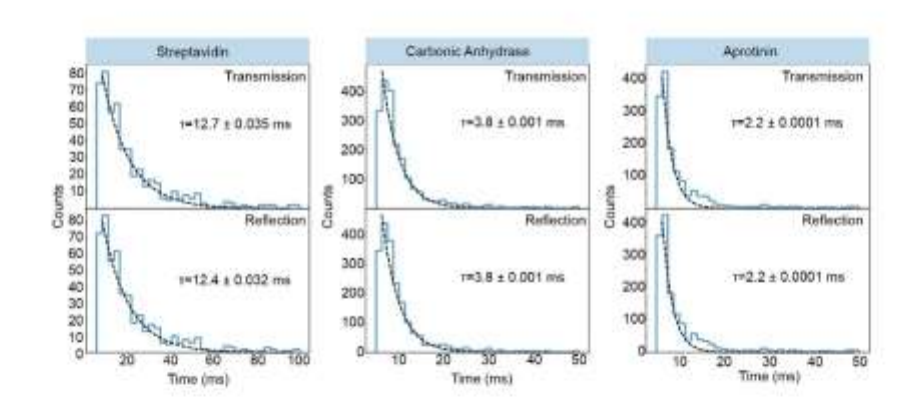
Extended Data Figures:



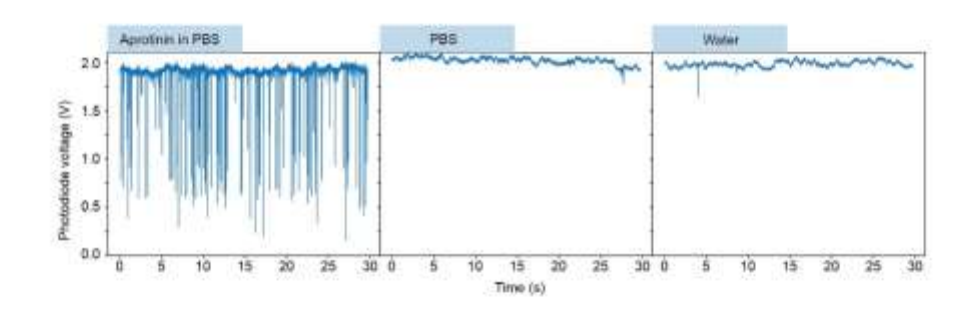
Extended Data Fig. 1 Zoomed in view of single-molecule signals. Representative 44 ms traces of proteins Streptavidin, Carbonic Anhydrase, Aprotinin and Myc-tag perturbing the cavity mode in both transmission and reflection. Data collected in cavity one.



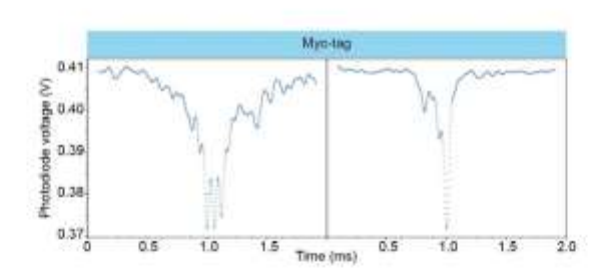
Extended Data Fig. 2 Linearity of peak count with concentration. Number of detected peaks induced by Myc-tag as a function of the protein concentration. Error bars represent the standard deviation across datasets. This scaling demonstrates that the peaks are induced by interactions between biomolecules and the cavity-mode. Data collected in cavity two.



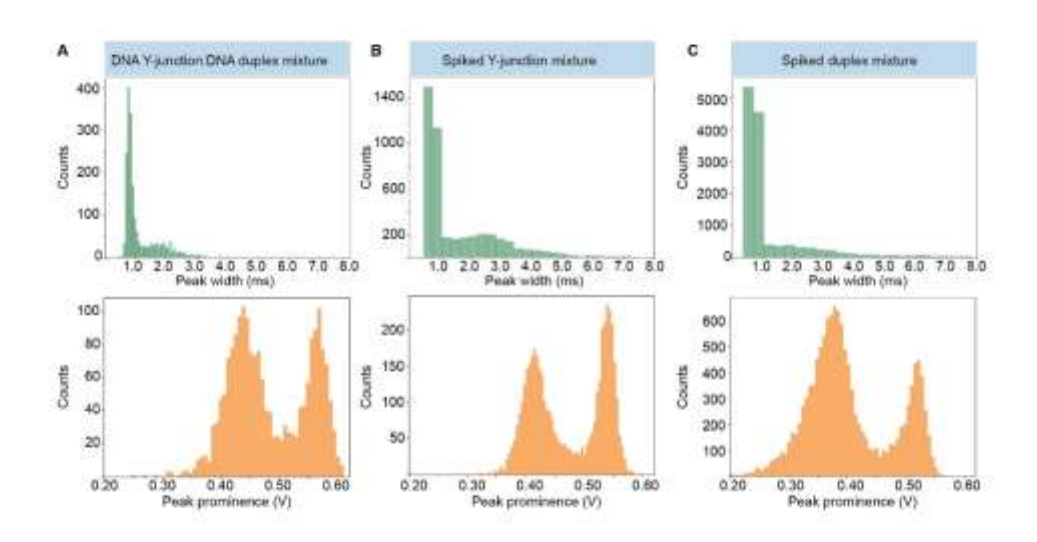
Extended Data Fig. 3 Poisson distribution of single-molecule signal arrival times. Statistical analysis of the time intervals between single-molecule events for proteins Streptavidin, Carbonic anhydrase and Myc-tag. This analysis shows mono-expontential decays illustrating the underlying Poisson behavior of the experiment and providing evidence of single-molecule detection.



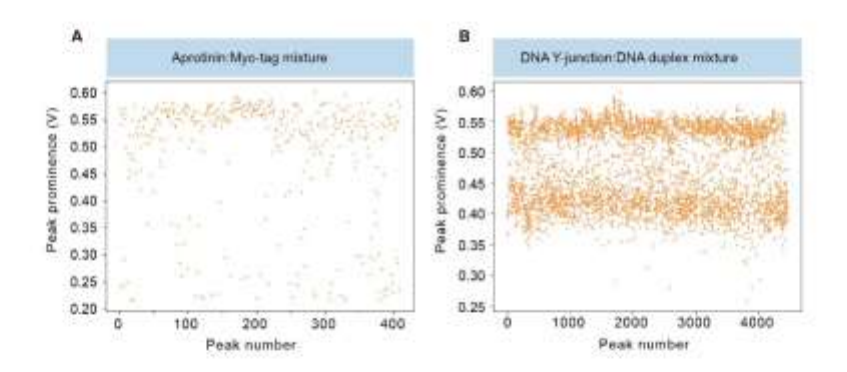
Extended Data Fig. 4 Detection of protein molecules in buffer. Single-molecule transients of aprotonin are readily observed in PBS buffer, while the pure PBS buffer and pure water are devoid of single-molecule signals.



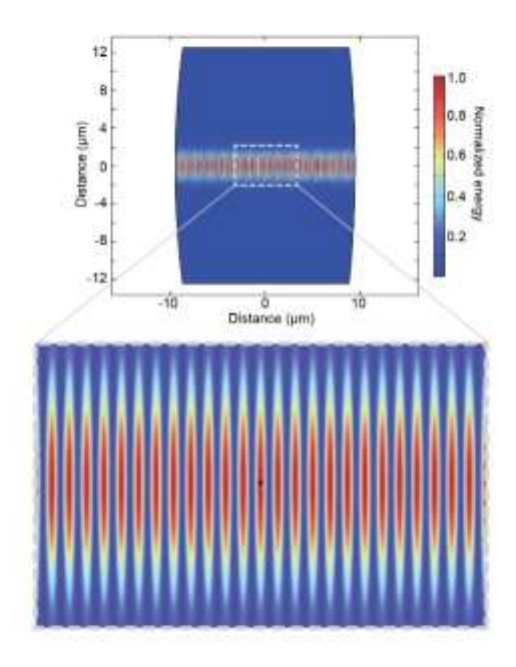
Extended Data Fig. 5 Detection of signals sampled at 500 kHz. Single diffusion events of <1 nm protein, Myc-tag, are resolvable with 2 µs temporal resolution. Representative single Myc-tag events collected with 500 kHz acquisition frequency. Data collected using cavity two at a concentration of 1 pM.



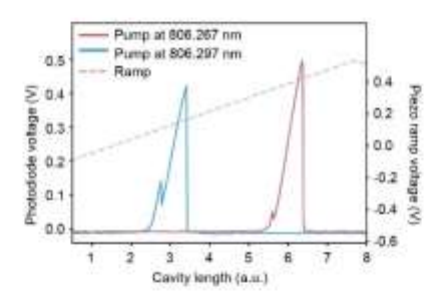
Extended Data Fig. 6 Histograms of detection events in mixtures. Histograms showing extracted temporal widths and peak prominences of transmitted signals of **a** a binary DNA Y-junction:duplex mixture (Table S 1), **b** the mixture spiked with additional amounts of the pure Y-junction and C) the mixture spiked with additional amounts of pure duplex.



Extended Data Fig. 7 Staggered detection from mixtures. Scatter plots of peak prominence vs peak number showing consistency of molecular populations throughout the duration of an experiment and minimal cavity mode wandering for **a** a binary mixture of Aprotinin and Myc-tag and **b** a binary mixture of a DNA Y-junction and duplex (Table S 1).

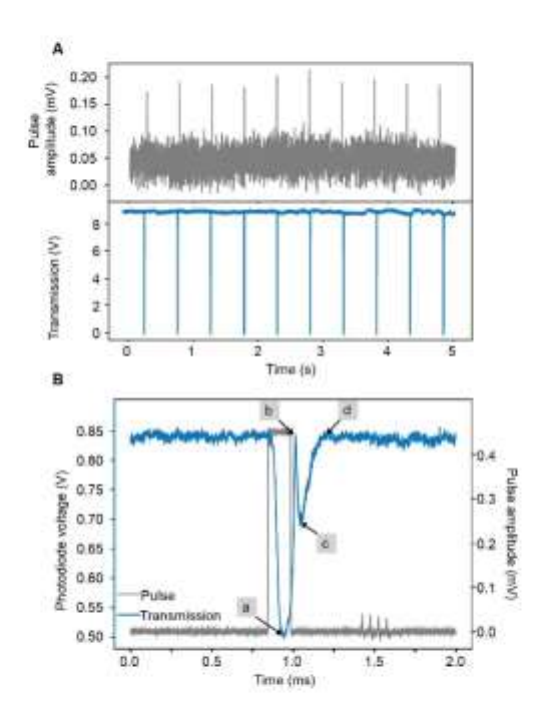


Extended Data Fig. 8 Simulation of microcavity resonant mode. Simulated cavity mode given the mirror properties of cavity one (Table S 5) showing the normalized square of the electric field which is proportional to the total energy stored in the cavity. The zoomed image shows a particle localized in an antinode in the center of the optical mode.



Extended Data Fig. 9 Photothermally distorted cavity resonance scan. Photothermal induced broadening of the transmitted cavity resonance in water, collected under cavity length tuning at two different pump wavelengths. The blue shift in pump wavelength shifts the resonance position to lower piezo ramp voltage, demonstrating that increased piezo ramp voltage corresponds to increased cavity length. Furthermore, the direction of the broadening is indicative of a negative thermo-optic coefficient of the medium as is expected

in water. Despite the low circulating power (5.5 mW), photothermal broadening was apparent and leveraged to enable the high sensitivity of this measurement. The smaller peaks originate from polarization splitting due to the birefringence of the cavity mode. Data collected with cavity four.



Extended Data Fig. 10 Replication of single-molecule-like signals by pulsing the length of the microcavity. a Transmitted intensity of locked cavity showing perturbations to the lock when voltage pulses are applied to the piezos at a frequency of 1 Hz. **b** The applied pulse, input-power and cavity locking parameters can be optimized to mimic signals induced by diffusing molecules. The step up voltage (gray) produced a steep reduction of the locked transmission signal due to the photothermal effect (a), this was followed by a brief recovery

to the locked state by the PI feedback loop (b) followed by a second descent of the transmission signal as the step-up voltage of the pulse shifts the cavity in the opposite direction (c), finally the PI control recovers the locked state (d). Data collected with cavity four.